UNIVERSITY OF CALIFORNIA,
IRVINE

Bio-inspired impact resistant coatings

THESIS

Submitted in partial satisfaction of the requirements for the degree of

MASTER OF SICENCE

in Materials Science and Engineering

by

Taige Hao

Thesis Committee:
Professor David Kisailus
Professor Stacy Copp
Professor Shen Dillon

2022

TABLE OF CONTENTS

LIST OF FIGRUES

LIST OF TABLES

ACKNOWLEDGEMENTS

I am extremely grateful to my advisor Professor David Kisailus, for his continued support and guidance. Without his encouragement and faith in my capabilities, this thesis and research would never have come to fruition. I genuinely thankful for his patience and trust in me, and I hope we can continue this relationship under the Materials and Manufacturing Department for my PhD program. In addition, I am also grateful for my committee members Professor Stacy Copp and Professor Shen Dillon, who were extremely accommodating while providing me with thoughtful and insightful feedback on my thesis. I am very fortunate to have these distinguished scientists teach and guide me through my journey as a master's student.

My deepest thanks are also extended to Dr. Wei Huang who showed me the way around his previous research, that my thesis is derived from, in addition to teaching me how to operate the instruments within our lab. The same can be said for Dr. Taifeng Wang who helped me stay focused on my research while also always being there for me both inside and outside of the laboratory. I wish them both continued success in their respective careers. Special thanks to my family, friends, and Meatball the cat who provided me with the food and emotional support.

I would like to acknowledge the support from the Air Force Office of Scientific Research Multi-University Research Initiative (FA9550 -15-1-0009) and the Air Force Research Laboratory (FA8649 -20-C-0314) for their generous funding and support. I must also thank the staff of the UCI IMRI and LEXI facilities for their management and trainings of the key materials characterization tools used in this thesis research.

ABSTRACT OF THE THESIS

Bio-inspired impact resistant coatings

By

Taige Hao

Master of Science in Materials Science and Engineering

University of California, Irvine, 2022

Professor David Kisailus, Chair

Protective coatings are commonly used to extend the service life of components or structures to provide a barrier against unexpected damage and harsh environments by improving the surface hardness, corrosion resistance, or oxidation resistance of materials. The objective of this research is to develop a biomimetic coating inspired by the impact resistant nanocomposite coating found on the dactyl club of the *Odontodactylus scyllarus* (i.e., the peacock mantis shrimp). These scalable sacrificial coatings would provide added impact protection to core structural components to extend their service life or to prevent catastrophic failure during impacts or collisions. This study will investigate the protective capabilities of a manmade analog comprised of inorganic (silicon carbide) nanoparticles embedded within an organic (chitosan) matrix. By varying particle loading, we can modulate the extent of energy dissipation and damping. Drop casting or spray deposition methods are used to yield thin-film coatings which localize damage and decrease penetration depth, thus protecting underlying substrates and improving overall impact resistance. The results show that up to a certain degree, additional particle loading improves impact resistance, which shows promise in potential implementations in the automotive, aerospace, and energy industries without adding significant weight.

Chapter 1: Introduction

1.1 Background of protective coatings

Protective coatings are ubiquitous in both our everyday lives and in many engineering or industrial applications. They can be highly specialized like the thermal barrier coatings (TBC) found in gas turbine engines or as simple as the paint on our walls. TBCs allow gas turbine engines to operate at higher temperatures, where they are more efficient [1]. Surface coatings, such as paints, provide a barrier against water intrusion, corrosion, UV damage, and wear, thus, extending the usable service of materials. These coatings help overcome the limitations of the base material.

Rapid corrosion of steel in aqueous environments can be greatly suppressed or controlled via the application of an anti-corrosion coating. These organic, inorganic, or metallic coatings function by three main mechanisms: barrier formation between the substrate and environment, inhibition of the corrosion process, and the coating acting as a sacrificial layer [2]. Typically, these coatings not only need to protect the substrate, but also must be resistant to wear, delamination, and spalling caused by the surrounding environment. Premature failure of the coating can lead to localized damage, which if left undetected or unaddressed, could lead to considerable inconvenience to humans and sometimes even the loss of life [2]. Therefore, before coatings can fulfill their deceptively straightforward purpose, they must first meet a wide range of criteria to ensure their own long-term performance.

A new direction for protective coatings is erosion resistant coatings for composite materials. Glass and carbon fiber composites offer a unique combination of high strength to weight ratio, fatigue resistance, and corrosion resistance, which makes them especially

appealing in engineering and structural applications. Their labor and resource intensive manufacturing process-which increases their cost compared to traditional materials-further emphasizes the need to maximize the service life of composite structures. For example, the leading edge of wind turbine blades is frequently eroded by the sand, water, and hailstones in the surrounding environment and can even be subjected to collisions with birds [3]. This causes a 6-500% increase in drag, which could result in a 25% loss of power generation annually[4]. To maintain the efficient performance of these turbines, commercially available products such as 3M Wind Blade Protection Coating W4600 have been developed to act as a sacrificial coating to resist erosion, have good adhesion, and have long lifespans.

1.2 Background on the peacock mantis shrimp

Through millions of years of evolution, nature has optimized and adapted the architecture and function of natural systems to improve survivability within a constantly changing environment. Over the past few decades, investigation into these natural systems has revealed numerous new material designs with widespread applications. One such example is the natural composite structure found within the mollusk shell, which acts as a strong and tough biological armor capable of resisting crush and penetration damage from predators[5]. However, despite their exceptional toughness, these shells are easily fractured by the high strain rate impacts imparted by the peacock mantis shrimp. Using its dactyl club, a hammer-like appendage, this powerful crustacean can accelerate its club over 10,000 m s^{-2} at speeds over 20 m s^{-1} to repeatedly apply forces up to 1,500 N as part of its

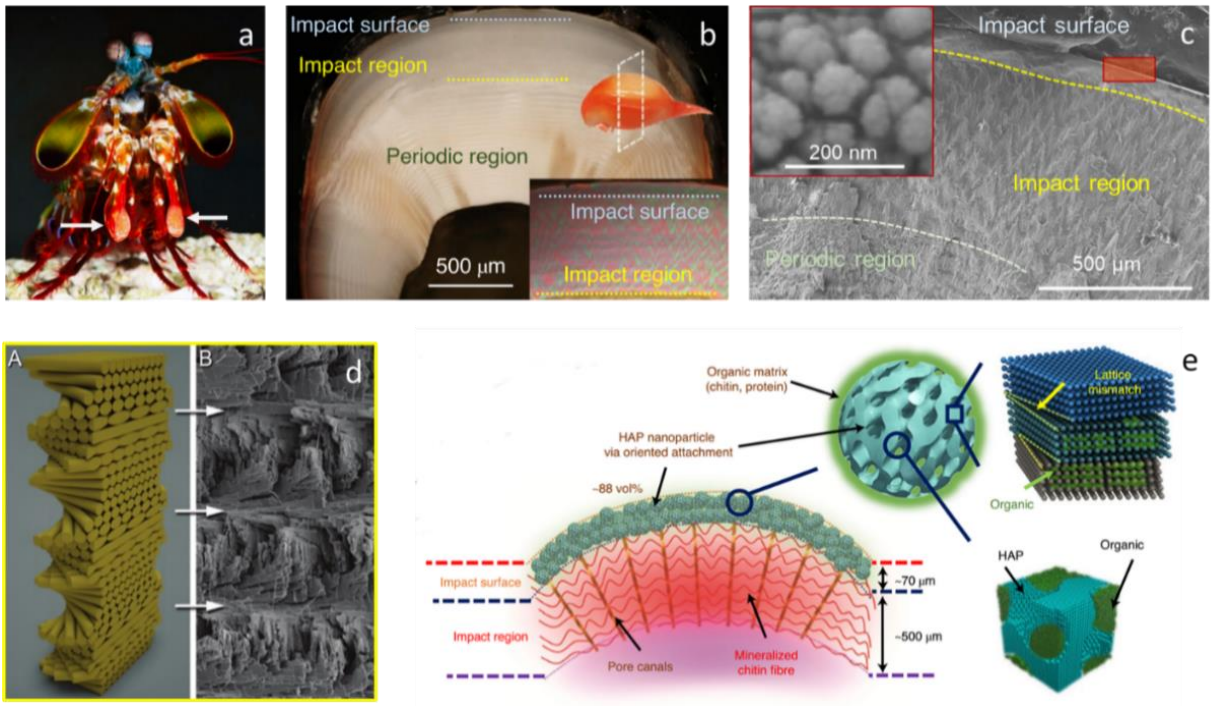

Figure 1.1: Architecture of the dactyl club of the mantis shrimp. (a.) Photograph of the mantis shrimp and its dactyl clubs, indicated by white arrows. (b.) optical micrographs of a transverse section of intermoulted dactyl club depicting the impact surface, impact region, and periodic region. (c.) SEM micrograph of transverse section of intermoulted dactyl club. Inset: nanoparticles (~60 nm in diameter) are found within the impact surface. (d.) schematic diagram of the helicoidal arrangement of α-chitin fibers derived from its corresponding SEM micrograph. (e.) Schematic of the dactyl club highlighting the location of the impact surface and its hierarchical nature[6].

predatory nature and ritualized fighting[6]. The exceptional toughness of the dactyl is attributed to a multi-regional structure consisting of a helicoidal arrangement of α-chitin fibers embedded in a mineral matrix (periodic region), an intermediate "impact region" consisting of a herringbone-like structure of nanocrystalline hydroxyapatite (HAP) mineralized chitin fibers[8], and a dense layer of ~88% volume bi-continuous HAP nanoparticles (~65.5± 15.4 nm) embedded in an organic matrix (impact surface)[6].

The area of interest for this work is the nanocomposite coating found in the impact surface region of the dactyl club. Here, mesocrystalline HAP nanoparticles are assembled from small highly aligned nanocrystals guided by the biomineral templating proteins. Because of this unique templated mineralization process, these HAP nanoparticles have an

interpenetrating phase of chitin and protein matrix, which allow them to respond elastically under low strain rates and fracture under high strain rates. In situ TEM compression tests on individual HAP nanoparticles separated from the club reveal a total energy dissipation of 6.23×10^{-24} nJ until particle failure. The energy dissipation density is ~4.55 nJ μm^{-3}, which is an order of magnitude greater than the bioceramic armor of the windowpane oyster (*Placuna placenta*) previously reported by Li et al. (~0.290 nJ μm^{-3})[5]. The blue, red, and black curves show three continuous loading cycles of a single particle where the plateaus on the curves indicate cracking events and particle breakage (indicated by arrows). The nanoparticle's ability to recover to its original shape after ~80%

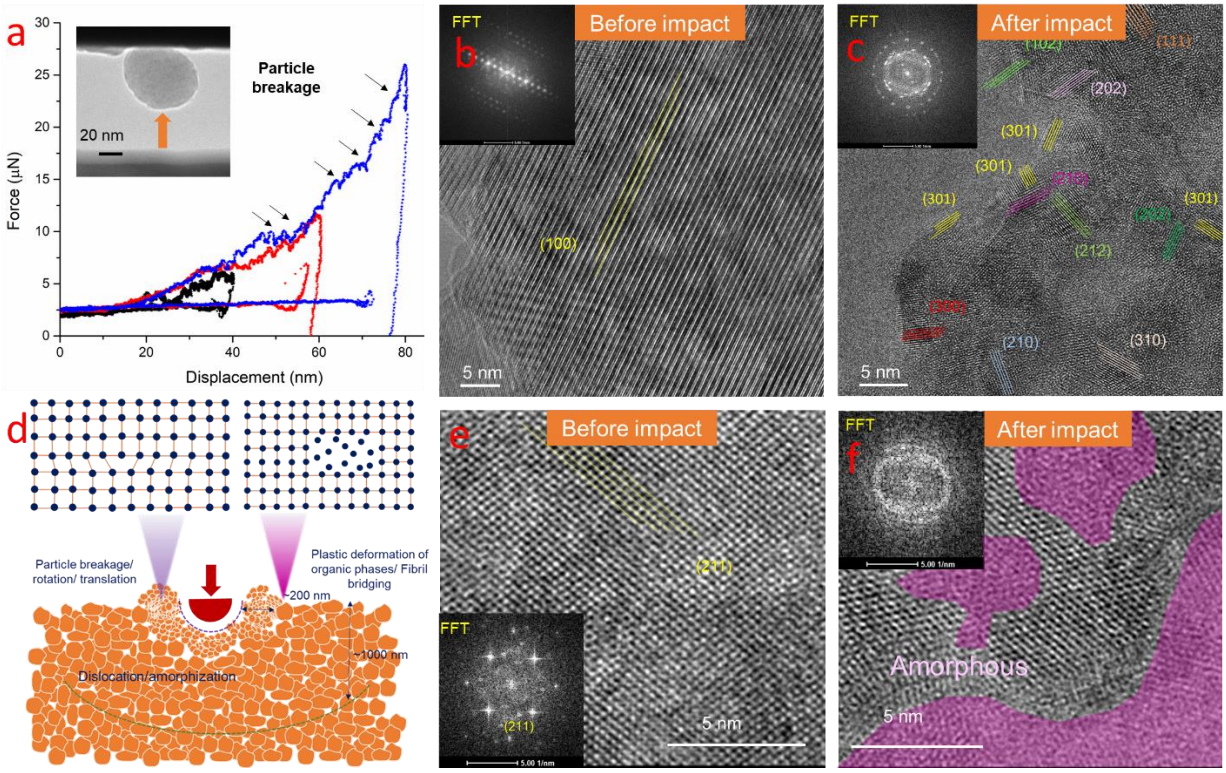

Figure 1.2: (a.) results from in situ TEM compression tests of three bicontinuous HAP particles obtained from the impact region of the dactyl club. Modification of the ordered (100) grains (b.) before the impact and (c.) subsequent rotation. (d) Schematic diagram depicting energy dissipation mechanisms (e-f.) Impact induced amorphization of the (211) Particle fracture was confirmed by comparing the SAED patterns of the specimens before and after impact [6].

compression is attributed to the bi-continuity of the hydrated organic networks, which provides added stiffness and strength over structures without integrated phases. This nanocomposite coating helps protect the dactyl club and prolong its useable lifespan by localizing damage and reducing penetration depth via particle fracture, translation, and rotation, as well as amorphization and generation of dislocations within the mineral phase as shown in Figure 1.2[6]. This natural system is the inspiration for the presented research. To emulate the mantis shrimp's coating as closely as possible, we used chitosan as the matrix material for our analog.

1.3 Chitosan films

Chitosan comes from the N-deacetylation of chitin, which is considered the second most abundant natural amino polysaccharide after cellulose. It can be sourced from the waste exoskeletons of crustaceans such as shrimp, crab, and lobster of which thousands of tons are produced by the seafood industry[10]. Its high abundance combined with its biodegradability, biocompatibility, and versatility[11] has garnered the attention of many researchers who have found uses for chitosan in applications ranging from food packing materials, drug delivery vehicles, and even applications for water treatment.

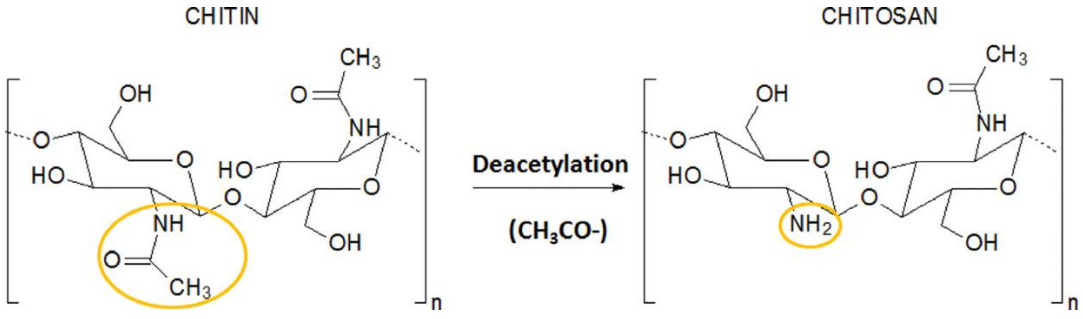

Figure 1.3: Chemical structure of chitin and chitosan after N-deacetylation[9].

Research in chitosan-based films has revealed that there is a wide range of mechanical properties due to the different characteristics of the chitosan (deacetylation degree, molecular weight) used, the solvent used to obtain the film, the chitosan content of the film, the storage time, and the measurement conditions before and during the test procedure[11]. The general trend presented in table 1 suggests chitosan films formed using higher molecular weights have high tensile strength and low percent elongation. The solvent can also have a significant effect on the film's strength and toughness. It is suggested that films formed using acetic acid are tougher than those formed using citric, lactic, or malic acid. Acetic acid can better dissolve chitosan of higher molecular weight,

Composition	Acid used	Chitosan properties	Conditions	Tensile strength (MPa)	Percent of elongation (%)	References
Chitosan 2%	Acetic	DD 95%	25 °C	68.8–50.2	7.6–5.5	Park et al. (2002)
	Citric	Mw 37–920 kDa	50% RH	6.7–17.4	41.9–117.8	
	Lactic			17.1–62.6	19.6–31.1	
	Malic			27.4–62.4	17.8–29.9	
Chitosan 1%	Acetic	Mw 150 kDa	25 °C	87.68	–	Li et al. (2010)
			20% RH			
Chitosan 2%	Acetic	DD 80%	25 °C	49.6–59.4	5.40–8.35	Srinivasa et al. (2004)
		Mw 100 kDa	50% RH			
Chitosan 2%	Acetic	DD 78%	–	55.6	8.0	Srinivasa et al. (2003)
		Mw 100 kDa				
Chitosan 1%	Acetic	DD 78%	–	39.1	10.84	Srinivasa et al. (2007)
		Mw 200 kDa				
Chitosan 1%	Acetic	High Mw	25 °C	61.8	4.59	Leceta et al. (2013)
			50% RH			
Chitosan 1%	Acetic	Low Mw	25 °C	55.8	4.58	Leceta et al. (2013)
			50% RH			
Chitosan 2.5%	Acetic	DD 85%	25 °C	~10.0	~58.0	Bof et al. (2015)
		Low Mw	60% RH			
Chitosan 2.5%	Acetic	DD 85%	25 °C	~18.0	~85.0	Bof et al. (2015)
		Medium Mw	60% RH			
Chitosan 2.5%	Acetic	DD 85%	25 °C	~60.0	~5.0	Bof et al. (2015)
		High Mw	60% RH			

Table 1: Table displaying the differing tensile strength and percent elongation for chitosan films prepared using differing solvents, deacetylation degree, and molecular weight[11].

which results in lower molecular volume with more intermolecular interactions[10]. Furthermore, chitosan can be combined with other additives such as plasticizers, other polysaccharides, proteins, and lipids to modulate its mechanical and barrier properties. This provides an opportunity for a tunable mechanical matrix system.

1.4 Current methods to form chitosan films

Chitosan films can be formed by drop casting[11], compression molding[12], or slot die casting[13]. The drop casting method is most used due to its accessibility and ease of use. However, both drop casting and compression molding are not capable of making large or continuous chitosan films., which is desirable in applications where chitosan is presented as an alternative to single use plastics.

Drop cast chitosan films are typically prepared by pouring a prepared 1-2% wt. chitosan solution into a petri dish or other flat container and evaporate the solvent by placing it into a drying oven or environmental chamber. After drying, a formed chitosan film can be peeled off from the substrate. The thickness can be controlled by varying the amount of solution placed into the container.

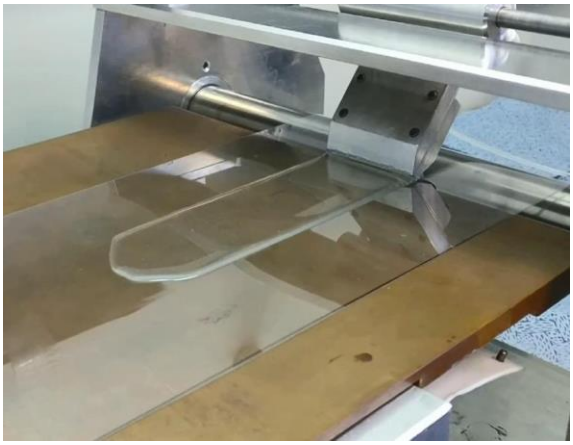

Figure 1.4: Picture depicting the slot-die apparatus used by Premble et al. to extrude continuous chitosan thin films[13].

Thin chitosan films produced via compression molding begin with the formation of a chitosan dough. Chitosan power is mixed with an acid and a minimal amount of water to form a dough. After homogeneous hydration, this dough is placed between two aluminum plates heated to 125°C and pressed at 2.5MPa to form chitosan films[12].

Slot-die casting can form continuous thin films by extruding chitosan solution through a die onto a PET substrate heated to 50°C. Using this method, Premble et al. was able to produce films 20-25μm thick[13].

Chapter 2: Drop cast coating deposition on glass substrates

2.1 Objective

To improve the toughness of the dactyl club, the mantis shrimp has developed an optimized impact resistant coating consisting of ceramic particles embedded within an organic matrix. This nanocomposite coating serves a dual purpose, to protect the dactyl club from catastrophic failure caused by the local stress concentrators during high energy, high strain rate impacts while simultaneously being stiff and hard enough to efficiently transduce the impact energy to its prey. Within this optimized system, the chitin and protein matrix act as a binder for the HAP nanoparticles, while also providing elasticity and a potential source of damping to enhance the toughness. The HAP nanoparticles enhance energy transduction by increasing the stiffness and hardness of the coating. We hypothesize the primary toughening mechanism is via the rotation, translation, and fracture of particles within the matrix.

In this chapter, we will focus on the replication of the mantis shrimp's impact resistant nanocomposite coating with synthetic analogs to systematically study the toughening mechanism as a function of particle loading within a polymeric matrix. To accomplish this, we have created a nanocomposite thin film comprised of inorganic ~60nm spherical silicon carbide (SiC) nanoparticles embedded within an organic chitosan matrix. SiC was chosen to replace the HAP found within the natural system due to its wide availability at nanoscale sizes, high hardness, and abrasion resistance.[14] To replace the chitin and protein matrix in the mantis shrimp, chitosan was chosen as it is the deacetylated form of chitin. Despite chitin's wide availability, its poor solubility limits its applications[9]. Removing the acetyl group from chitin to form chitosan, as shown in Figure 1.3, makes it soluble in a variety of acids through the protonation of the remaining amino

groups[11], [15], [16]. To better understand the role of particle loading in changing the stiffness and hardness, quasi-static nanoindentation was used to determine the reduced modulus and hardness. To test the protective capability as a function of particle loading, nano impact testing was performed to impart high strain rate damage to the coating. Scanning electron microscopy of the impact craters was employed to understand the energy dissipation mechanisms and quantify the coating damage.

2.2 Experimental Procedure

2.2.1 Chitosan solution and SiC suspension preparation

The drop casting method was used to fabricate the films. An aqueous solution (1% v/v) of acetic acid was first prepared in 50mL of DI water, then heated to 50°C with vigorous 1000RPM stirring. To create 1% w/v chitosan solution, 0.5g of low molecular weight chitosan powder (50-190kDa Sigma 448869-50G) was added once the solution had

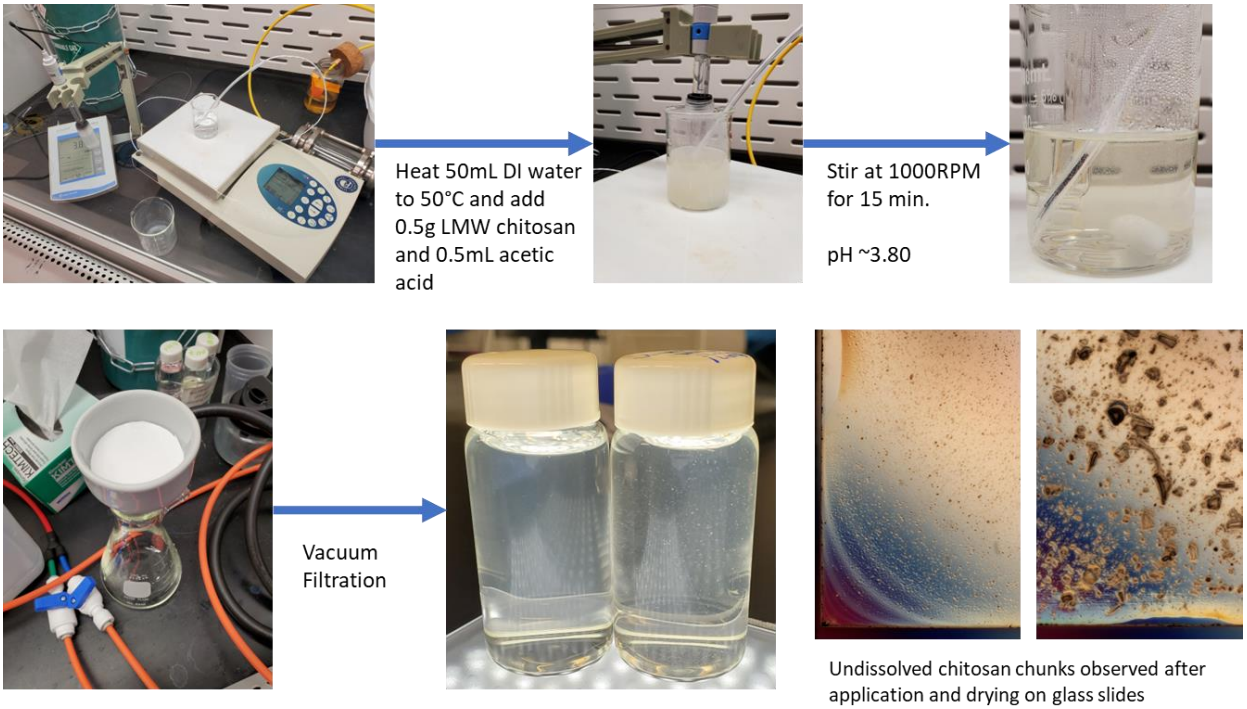

Figure 2.5: Process used to make 1% w/v chitosan solution and with (left vial and micrograph) and without(right vial and micrograph) filtration respectively.

reached 50°C and was left stirring for 15 minutes. The final pH of the solution was ~3.80. After the chitosan solution had become mostly homogeneous, it was then vacuum filtered through Fisher Scientific P8 filter paper (09-795B) to remove any impurities.

To prepare 1% w/v SiC suspension, 0.3g of ~60nm "spherical" SiC nanoparticles were added to 30 mL of DI water. To prevent agglomeration, 30µL of Hydrochloric acid was added, then the prepared suspension was tip sonicated for 10 minutes with a 0.75 on cycle using a Hielscher UP100H with the MS10 tip. The pH of the final solution was around ~1.90

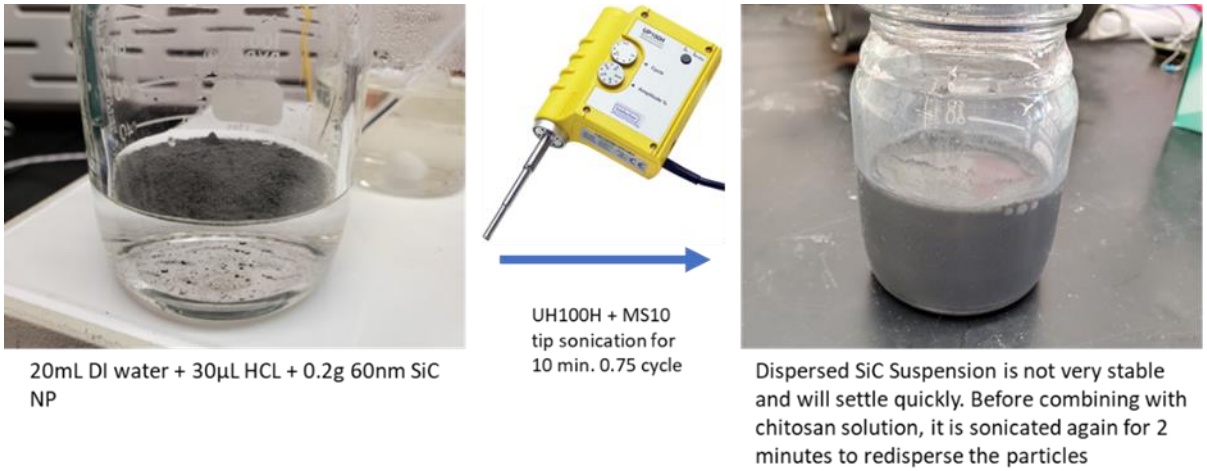

Figure 2.6: Process used to make 1% w/v silicon carbide (SiC) suspension.

The prepared SiC suspension and chitosan solution were then combined at different ratios to achieve the desired volume percent of SiC loadings (30, 50, and 80 vol. %). For example, to make a 50% volume fraction SiC solution, 5mL of the chitosan solution was combined with 5mL SiC suspension. The combined solution was then tip sonicated for 5 minutes by the Hielscher UP100H with the MS3 tip to ensure good mixing and homogeneous dispersion of the SiC nanoparticles within.

2.2.2 Glass substrate preparation and coating deposition

Glass microscope slides 75mm x 25mm were sectioned into 25mm x 25mm coupons using the score and snap method. To remove oils and organic residue, the prepared coupons were then cleaned with 200 proof ethanol and dried using an oil free and moisture free air source. Before solution deposition, the prepared suspensions were again sonicated to mitigate any settling that may have occurred. 0.4mL of the prepared coating was then deposited using a micropipette. Due to the surface tension of the droplet as shown in Figure 2.7, the coating was then spread -with a micropipette tip- to cover the entire surface and left to dry overnight.

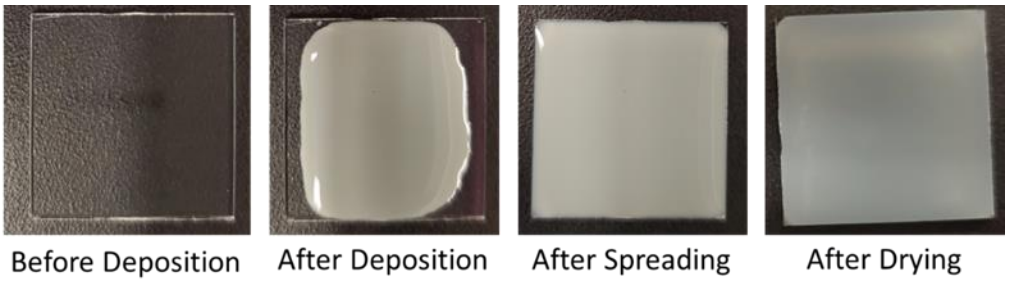

Figure 2.7: Pictures showing the drop casting process to form thin films on a glass substrate.

2.3 Characterization

2.3.1 Nanoindentation

Quasi-static nanoindentation was performed at room temperature using a TI-950 Triboindenter (Hysitron, USA) with a Berkovich diamond indenter. The load profile used in all indentation tests is trapezoidal with loading and unloading periods of 5 seconds and peak load periods of 5 seconds. To clarify the substrate effect and the indentation size effect (ISE), peak indentation loads from 5 – 50mN were used on the pure chitosan control sample. Analysis of the resulting data noted a significant increase in the substrate effect

between loads of 10mN to 20mN. Subsequent indentation maps of the surface were conducted using a 5mN peak load to minimize the substrate effect.

To measure the hardness and reduced modulus of the protective coatings, indentation maps of the coating surface were done in a 10 by 10 square array spaced 80 micrometers apart to minimize the influence of surface roughness and strain fields from neighboring indents. Prepared samples were first superglued to steel AFM stubs to facilitate mounting to the magnetic stage of the instrument. Indentation maps were performed on bare glass and pure chitosan to establish a baseline, and then again on quartz coated by 30%, 50%, and 80% vol. SiC protective coating. From these tests, we hope to determine the optimal ratio of toughness to stiffness, as it can greatly influence whether the applied impact energy is absorbed and dissipated by the coating or directly conducted to the substrate.

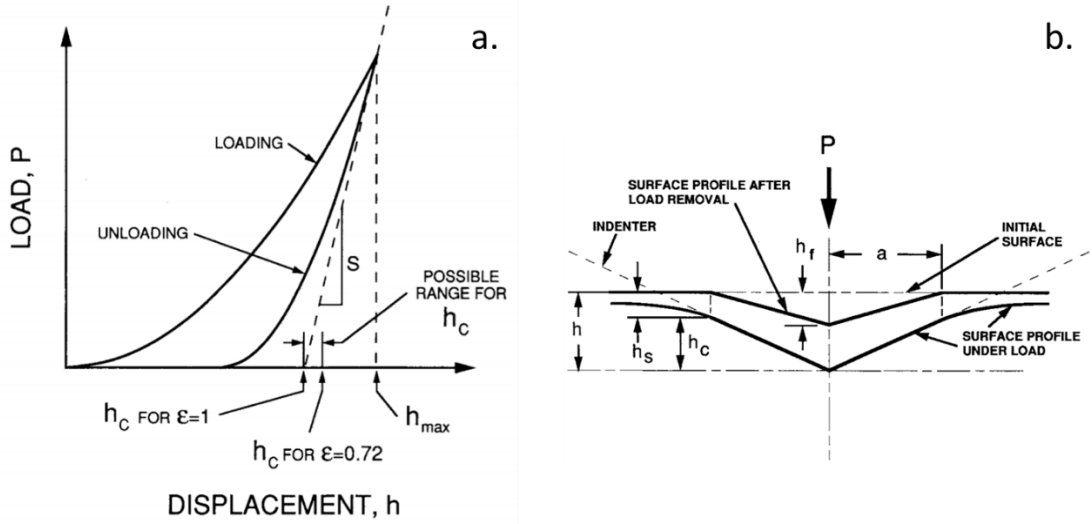

Figure 2.8: (a.) schematic representation of typical load vs indenter displacement curve indicating the quantities used in analysis and range for contact depth h_c and (b.) a schematic representation of a cross sectional view of the indentation process and the quantities used for analysis[17].

The unloading curve of each indent was used to calculate the hardness and reduced modulus following the Oliver-Pharr method[17]. The slope of the initial unloading curve $\frac{dP}{dh}$ represents the contact stiffness S. This, combined with the contact area A can be used in equation 1 to calculate the reduced modulus E_r .

$$E_r = \frac{\sqrt{\pi}}{2} * \frac{S}{\sqrt{A}} \quad (1)$$

The contact area A is determined by the tip area function $F(h_c)$, which relates the geometry of the indenter to the contact depth h_c. The contact depth is indicated in Figure 2.7b, where it is related to the total displacement h of the indenter into the sample minus the elastic displacement of the surface surrounding the indenter h_s as shown by equation 2.

$$h = h_c + h_s \quad (2)$$

Deflection of the surface near the indenter can be represented by equation 3, where the theoretical geometric constant for a Berkovich tip is $\varepsilon = 0.75$ and the max load is P_{max}.

$$h_s = \varepsilon * \frac{P_{max}}{S} \quad (3)$$

Upon unloading, the indenter is removed from the sample and the residual indent depth after elastic recovery is h_f. Figure 2.7b provides a schematic of the unloading parameters in addition to the load applied P, the final depth of the residual hardness impression, and the radius of the contact circle a. Hardness can be calculated using equation 4 where it is defined as the mean pressure the material can support under load.

$$H = \frac{P_{max}}{A} \quad (4)$$

2.3.2 Nano Impact

Characterization of the dynamic response of the protective coating was performed at room temperature using a Nanotest Vantage Platform 4 System (Micromaterials Ltd, Wrexham, UK). Unlike nanoindentation, this instrument can load the material surface with strain rates several orders of magnitude higher. Both single and multiple nano-impact tests were performed using the low load (0-500mN) head with a 5mN accelerating load and a 10000 nanometer accelerating distance.

A series of 10 single impact tests were performed on each of the prepared samples using the dynamic hardness module and a 5μm diamond spheroconical tip. Before the

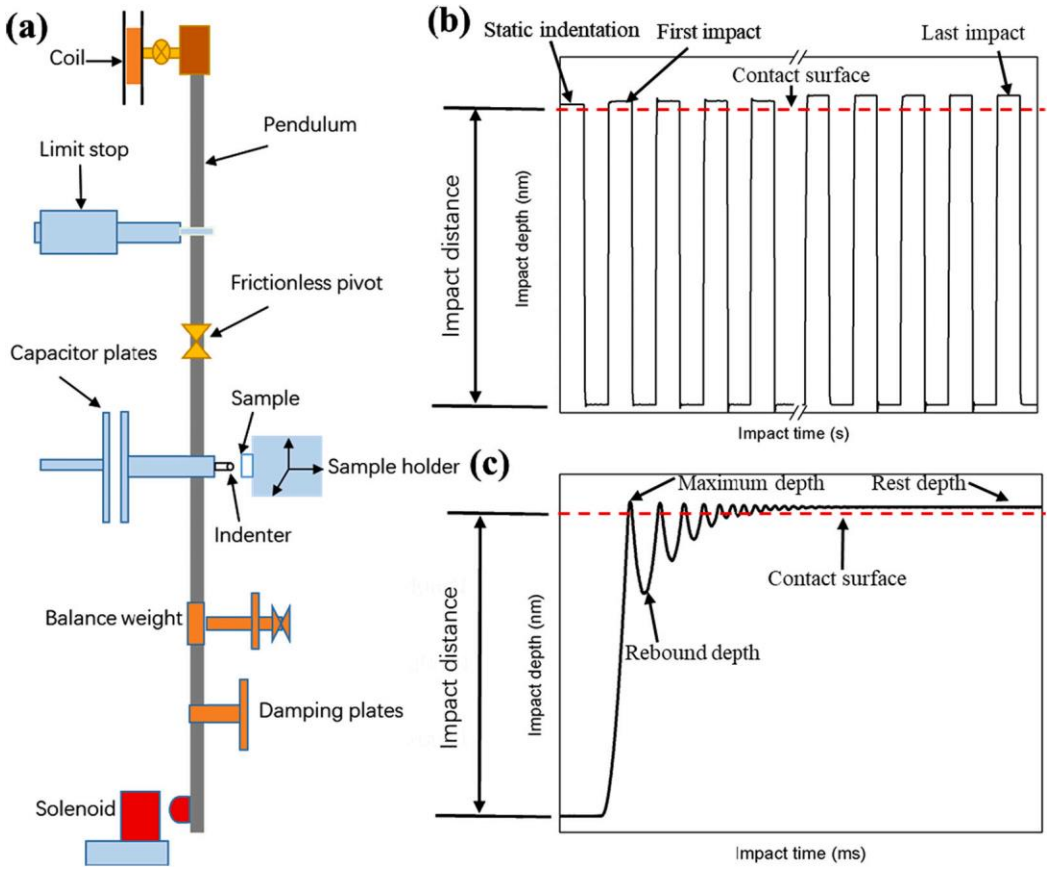

Figure 2.9: (a) Schematic illustration of the pendulum configuration of the NanoTest system for impact testing, (b) typical impact depth vs time curves for the "Multiple Impulse" mode, and (c) typical impact depth-time curves for "Dynamic Hardness" mode from Shi et al. [18].

indentation process begins, the instrument first finds the surface of the sample by having the indenter contact the surface at a very low force to establish the zero-displacement point. While the pendulum is retracted by the bottom solenoid, the desired accelerating load at the top of the pendulum is applied. Upon release of the bottom solenoid, the indenter tip then accelerates towards the sample surface. The velocity of the indenter will then increase gradually, which increases the kinetic energy of the indenter until contact with the sample surface. Here, the tip penetrates the sample until the velocity decreases to zero and the kinetic energy is transferred into reversible elastic work, irreversible plastic work, and other energy dissipation mechanisms such as frictional work and heat loss. Subsequent release of the stored elastic energy will cause the indenter tip to rebound until the tip comes to rest on the sample. Throughout this process, the instantaneous change of the probe displacement as a function of the impact time is measured and recorded (Figure 2.9c).

In addition to single impacts, multiple impacts within the same location were also performed using the multiple impulse module. Here, the same process as single impact tests occurs, but 100 cycles are completed before the indenter tip moves to the next location. Each impact cycle was completed in 4 seconds, including 2 seconds with the load applied and 2 seconds of the load removed. The total time of each test was 400 seconds, which corresponds to 100 cycles. For these cycles, the evolution of the impact depth as a function of impact cycles is recorded (Figure 2.9b). For both dynamic hardness and multiple impulse, ten regions spaced 100 micrometers apart were done to account for localized variability in the coatings and prevent the overlap of adjacent strain fields from previous impacts.

2.3.3. Scanning Electron Microscopy

The homogeneity of the coating, characterization of energy dissipation mechanisms, and damage to the coating from nano-impact testing were imaged using the Tescan GAIA 3 SEM at the UC Irvine Materials Research Institute (IMRI). An accelerating voltage of 10kV and a spot size of 5 were used. Before imaging, all samples were coated with a 5nm iridium (Ir) coating using an EMS 150T sputter coater to reduce the electron charging effect. The thickness of the coating was also measured by imaging the cross section of 80% volume SiC film where it delaminated.

2.4 Results and Discussion

2.4.1 Substrate Effect and Interphase Effect

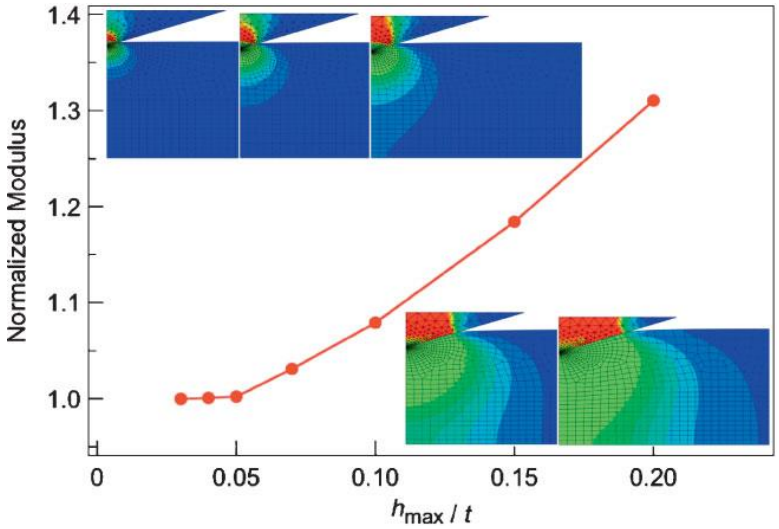

Figure 2.10: Elastic modulus from nanoindentation simulations normalized by input modulus (E = 2.7 GPa) as a function of h_{max}/t (using ratio of elastic modulus to yield strength = 20). Insets are contour plots of the stress at the indent depth ratios 0.03, 0.05, 0.07, 0.15, and 0.20. For $h_{max}/t < 0.05$, a significant stress field does not reach the rigid substrate[19].

Nanoindentation is widely used for measuring the mechanical properties of materials at very small length scales as shallow as 20 nanometers. The ability to probe at such fine scales makes nanoindentation especially suited for characterizing the mechanical properties of thin films, as the properties can be measured without removal from the substrate[20]. However, when characterizing these thin films, the effect of the substrate

can inflate the calculated reduced modulus and hardness values [19]–[21]. Finite element modeling by S. Watcharotone et al. in Figure 2.10 reveal that for low penetration depths, the stress field generated by the indenter tip does not reach the substrate. This is in line with previous studies demonstrating that the substrate effect can be mostly avoided at penetration depths less than 10-15% of the total film thickness [20], [21]. As the penetration depth increases, the stress field increases towards the substrate. With increasing interaction between the stress field and substate, the apparent modulus also increases significantly[19]. One way to minimize the substrate effect is to control the indentation peak load, which directly effects the indentation depth.

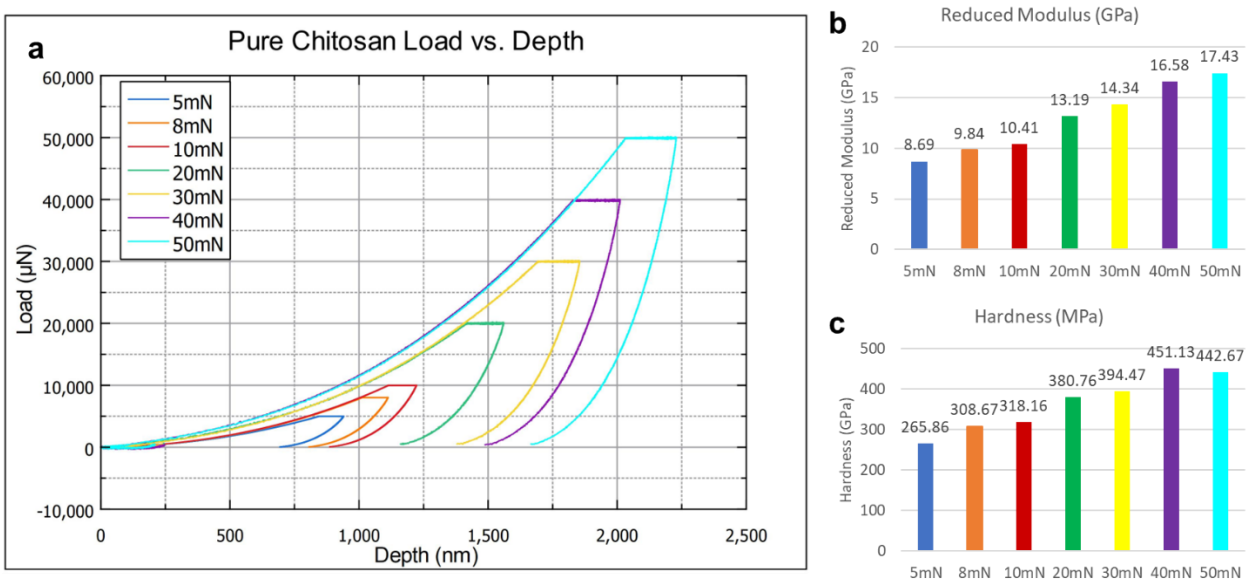

Figure 2.11: (a.) Depth vs. load curves for quasi-static indentation on pure chitosan coating with forces ranging from 5 – 50mN, (b.) Calculated reduced modulus and (c.) hardness using the Oliver-Pharr method.

For the pure chitosan control coating on the comparatively hard glass substrate, the influence of the substrate effect on the reduced modulus and hardness was tested. From a peak load range from 5 – 50mN, a penetration depth range of 940.42nm - 1955.36nm was observed. From the calculated reduced modulus data, there is a sharp increase in the reduced modulus from 10.41GPa to 13.19GPa at 10mN to 20mN peak indentation load.

This suggests that for peak loads greater than 10mN, the stress field generated by the indenter tip has significant interaction with the hard glass substrate, resulting in the apparent increase in modulus.

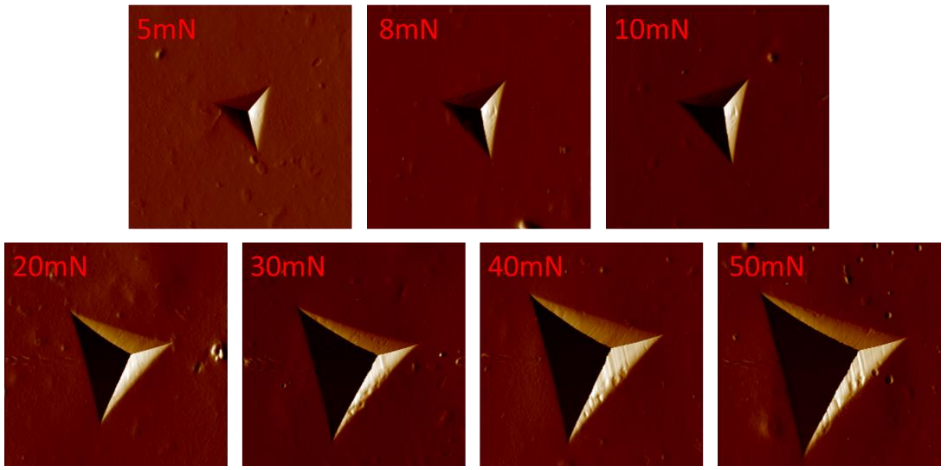

Figure 2.12: Scanning Probe Microscopy micrographs of the indent after indentation ranging from 5 – 50 mN showing sharp and well-defined Berkovich indenter geometry without pileup. Each image is 30 µm x 30 µm.

The same jump can also be observed in the hardness values at 10-20mN peak loads. The apparent hardness of the coating increases from 318.16MPa to 380.7MPa and continues to 442.67MPa at 50mN peak load. According to equation 4, the hardness is calculated by dividing the applied load (P_{max}) by the contact area of the tip (A). As explained by Tsui et al., an underestimation of the true contact area, due to pileup, can also inflate the apparent modulus and hardness. Scanning probe microscopy of the indentation impressions reveals sharp triangular indentation patterns with well-defined edges rather than bowed-out edges, indicative of the extra contact area from pileup. Although differences in the true contact area and the ideal contact area can affect the apparent hardness, it does not seem to play a significant role in our samples. Another mechanism that may contribute to the increased hardness is the interphase effect at the substrate-film interface where the polymer dynamic is limited by the interactions between the two. As the

stress field progresses downward toward the substrate, the interaction of the stress field with the interphase can also increase[19], [22]. To minimize the deviation in apparent modulus and hardness due to the substrate effect, all subsequent indentation mapping was performed with a 5mN peak load. For samples tested at 5mN (Figure 2.13), the average film thickness was measured to be ~ 7 µm (Figure 2.14f). With penetration depths peaking at ~0.7 - 1 µm the substrate effect should have no significant contribution

2.4.2 Nanoindentation

Using the Oliver Pharr method described above, the indentation load-displacement data was analyzed to determine the reduced modulus and hardness values for each of the

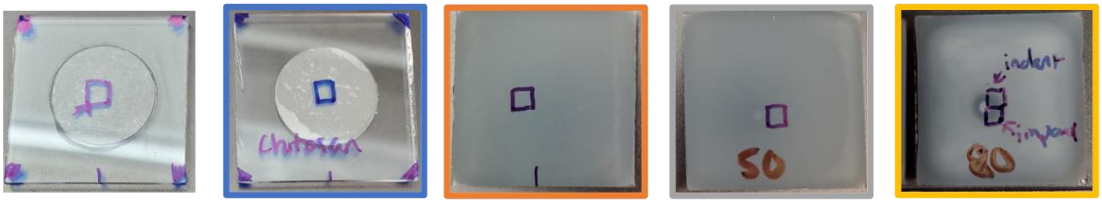

	Glass Control	Pure Chitosan	30 vol% SiC	50 vol% SiC	80 vol% SiC
E_r (GPa)	73.462 ± 0.819	8.962 ± 0.090	10.723 ± 1.235	11.97 ± 1.357	9.877 ± 1.681
H (GPa)	6.939 ± 0.142	0.287 ± 0.004	0.355 ± 0.069	0.350 ± 0.061	0.194± 0.046
Depth (nm)	154.203 ± 1.684	814.366 ± 6.19	740.059 ± 74.673	743.364 ± 65.727	1015.050 ± 114.898

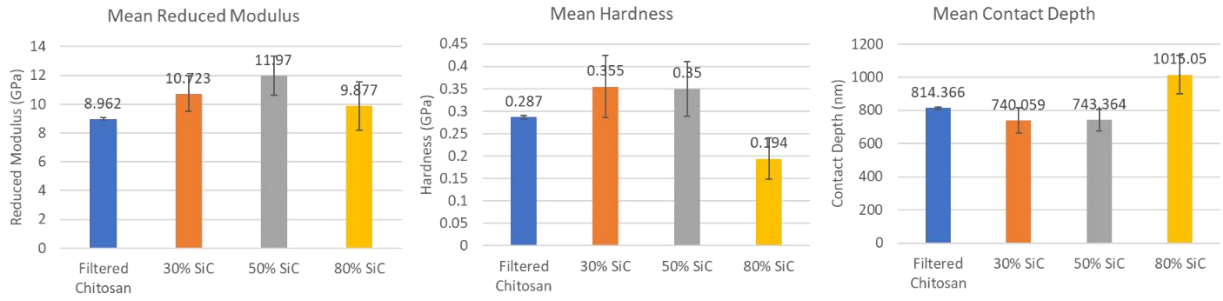

Figure 2.13: From top to bottom, pictures of the tested samples with squares indicating the location of both nanoindentation and nano impact testing, reduced modulus (E_r), Hardness (H), and contact depth as averages of 100 indents, and plots of the above data for easier visualization.

hundred indents. The data shown in Figure 2.13 show that the stiffness and hardness of the SiC/Chitosan nanocomposite thin films are higher than that of pure chitosan. For 30% and

50% particle loading, there is a notable increase in hardness and stiffness. At 80% particle loading, the stiffness drops off significantly and the hardness is below that of the pure chitosan sample. For the glass control, the reduced modulus (E_r) and the hardness are close to the reported values for borosilicate glass[23]. These results indicate that the tip area calibration and instrument calibration are current and accurate at the time of testing.

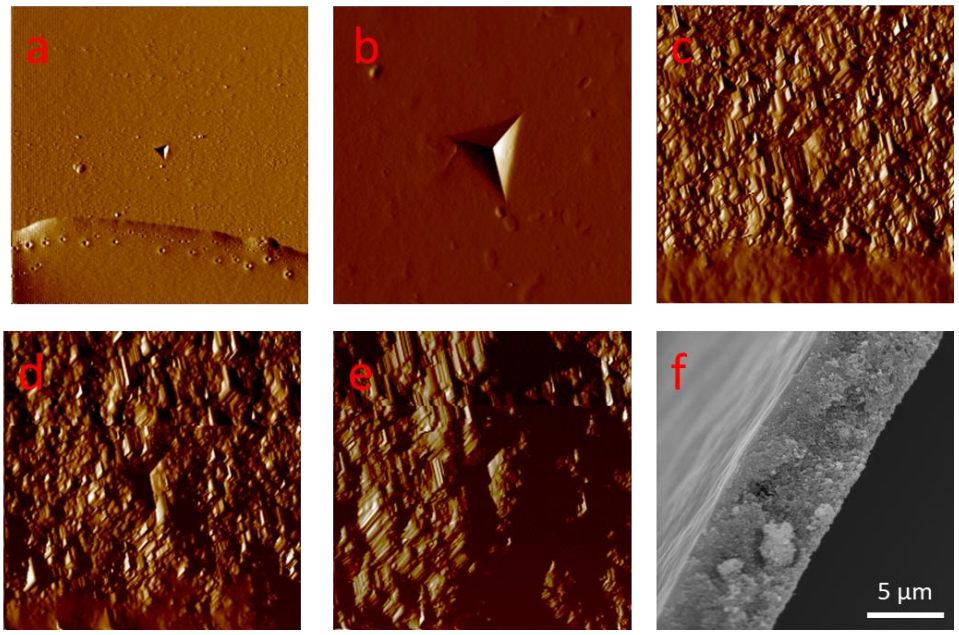

Figure 2.14: Scanning Probe Microscopy micrographs of the 5mN indent on (a.) glass substrate, (b.) pure chitosan, (c.) 30% volume SiC, (d.) 50% volume SiC, (e.) 80% volume SiC and (f.) SEM cross section of the film shows a thickness of ~7 µm. For (c-e), the sharp "cube corner" like roughness shown is an artifact of the instrument and not representative of the actual sample topology.

From nanoindentation of pure chitosan films, the mechanical properties of the nanocomposite matrix material are established. The data for the reduced modulus, hardness, and mean contact depth can be seen in Figure 2.13 along with comparisons with pure class and different volume percent loading of SiC nanocomposites. One key thing to note is the relatively low standard deviation when compared to those with nanoparticles incorporated. The low standard deviation can be potentially explained by the reduced surface roughness and homogeneity when compared against SiC/Chitosan nanocomposite

films. Even when compared to the glass substrate, the surface roughness of the chitosan films is improved. Unfortunately, due to instrument limitations, the sharp “cube corner” bumps observed in the SPM maps of the SiC/Chitosan coatings are instrument artifacts as they are not observed under optical microscopy or SEM. Reducing the scanning speed did not yield any noticeable improvement either. The scans for the SiC/Chitosan samples are not perfect, but the increase in the size of the “cube corner” artifacts from 30-80% vol SiC loading does correlate with the increase in standard deviation for each sample’s reduced modulus.

The increase in modulus and hardness of SiC/Chitosan samples when compared to the pure chitosan sample can be attributed to a variety of factors such as phase co-continuity, particle percolation, and the interphase effect. In polymer nanocomposites, the nanoparticles themselves cannot form a continuous phase. They instead rely on the immobilized polymer phase attached to the nanoparticle surface, the interphase, to establish a continuous phase. Due to this dependence, the nanofiller-matrix adhesion at the particle interface also plays a critical role in the overall performance of the nanocomposite. Furthermore, if the adhesion between the nanofiller and matrix is poor, the fillers are more likely to agglomerate into clusters that establish defect centers where the stress transfer is poor[24]–[26].

Characterization of the SiC/Chitosan interface was done with TEM. TEM micrographs of a dilute sample of the prepared SiC/Chitosan are shown in Figure 2.15 starting with a schematic (Figure 2.15a) of the SiC nanoparticle surrounded by the chitosan interphase. The chitosan is attached to the SiC surface via hydrogen bonding and

electrostatic interactions and wraps around the entire particle. SEM micrographs of the SiC nanoparticles (Figure 2.15b) show that the size distribution is relatively consistent even if the particles themselves are not perfectly spherical as advertised by the supplier. Although the exact mechanism is not yet understood, theoretical calculations by Knauert et al. have shown that the shape of the nanoparticles used has a significant effect on both the mechanical properties and processing characteristics[27]. The presence of the chitosan interphase was determined by comparing the TEM micrographs of SiC nanoparticles with (Figure 2.15d) and without (Figure 2.15c) chitosan. For systems containing chitosan, an interphase of chitosan macromolecules can be observed as fringes surrounding the SiC

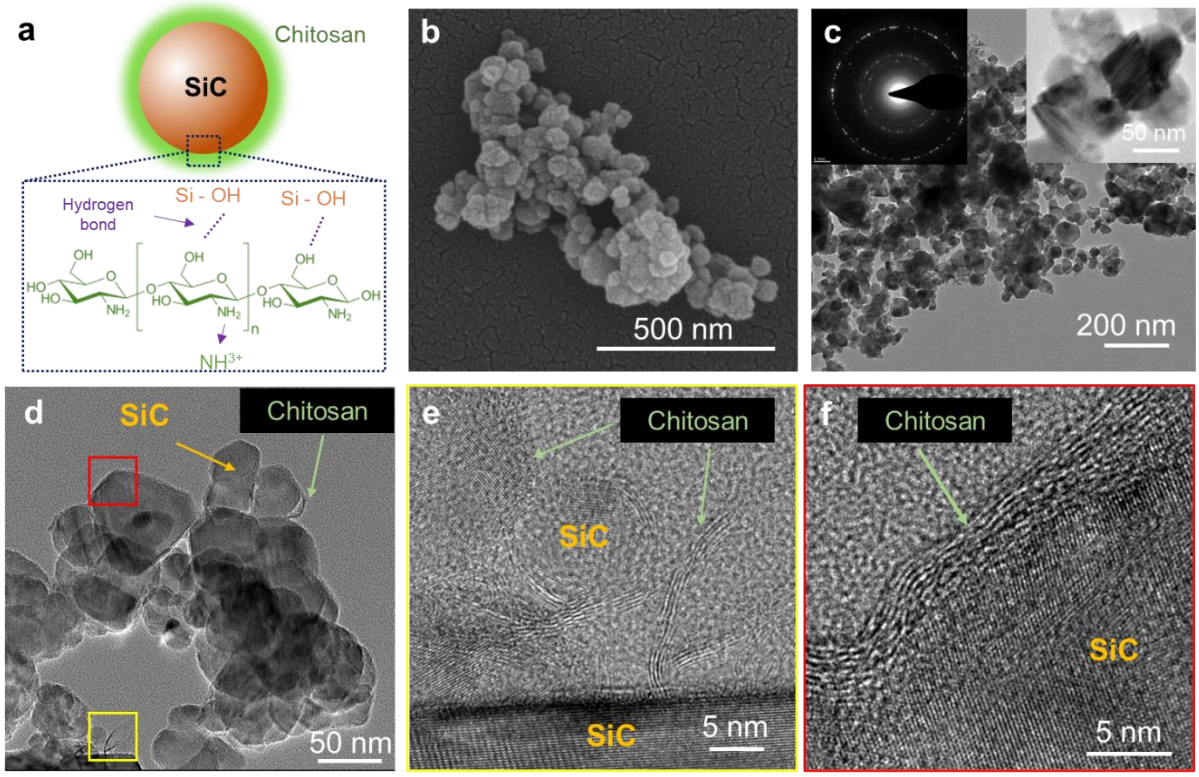

Figure 2.15 SiC/chitosan nanoparticle composites. (a.) Schematic showing chitosan macromolecules wrapping around SiC nanoparticles. (b., c.) SEM and TEM images show the original SiC nanoparticles. (d.) TEM image depicts the chitosan macromolecules wrapping around SiC nanoparticles forming SiC/chitosan nanocomposites. (e., f.) HRTEM shows the SiC and chitosan interface[6].

nanoparticles. Further investigation via HRTEM shows the attachment (Figure 2.15e) and interface (Figure 2.15f) between the chitosan interphase and SiC nanoparticles.

Due to the sole reliance on the chitosan matrix for phase co-continuity, the continuity of the chitosan co-continuous phase among the particles falls into question at higher nanoparticle loadings, as a drop-off of both hardness and modulus from 50 to 80% volume. SiC loading is observed. (Figure 2.13). The increase in coating stiffness at 30 and 50% volume loading and visual observation of the coating surface in the SEM micrographs provided in Figure 2.20 reveal a continuous chitosan phase up to 80% volume SiC loading. Here, the presence of the chitosan phase is greatly diminished. To a certain extent, the chitosan phase is still present within the 80% volume SiC coatings, within localized regions, and can somewhat interact/connect the immobilized chitosan interphases found on the surfaces of the SiC nanoparticles.

Particle percolation may also contribute to the observed increase in modulus and hardness. During indentation, as the film is compressed by the indenter tip, the SiC nanoparticles dislocate, rotate, and translate like the HAP nanoparticles found within the impact resistant coating of the mantis shrimp. It is during this movement of the particles within the matrix that they contact each other and eventually form a continuous path. This is called the percolation point [28]. The critical value at which there is enough binder holding the particles together to form a rigid structure is called the rigidity percolation point[28]. A similar study on a sand-filled polyethylene composite by Verbeek demonstrated similar behavior. Like the SiC/Chitosan system, the modulus begins to increase around 30% volume particle loading, peaks at 50-60% volume, and drops sharply

approaching 80% loading. As more particles are introduced, the modulus increases gradually through the percolation point (0.6 vol. fraction polymer) and the particles begin to form a connected network through the polymer matrix. The modulus increases until the system becomes dominated by particle-particle interactions, where lack of interconnecting matrix and localized particle agglomeration lead to poor transfer of stress through the system. At 0.24 vol. fraction polymer in Figure 2.16a, the percolation point of the polymer matrix is reached. The disjointed connectivity of the polymer matrix around this point causes a sharp decrease in the modulus[28]. At 80% vol. SiC loading, the SiC/Chitosan system has just surpassed the rigidity percolation point where there is still a measurable increase to the reduced modulus when compared to pure chitosan. There is just enough

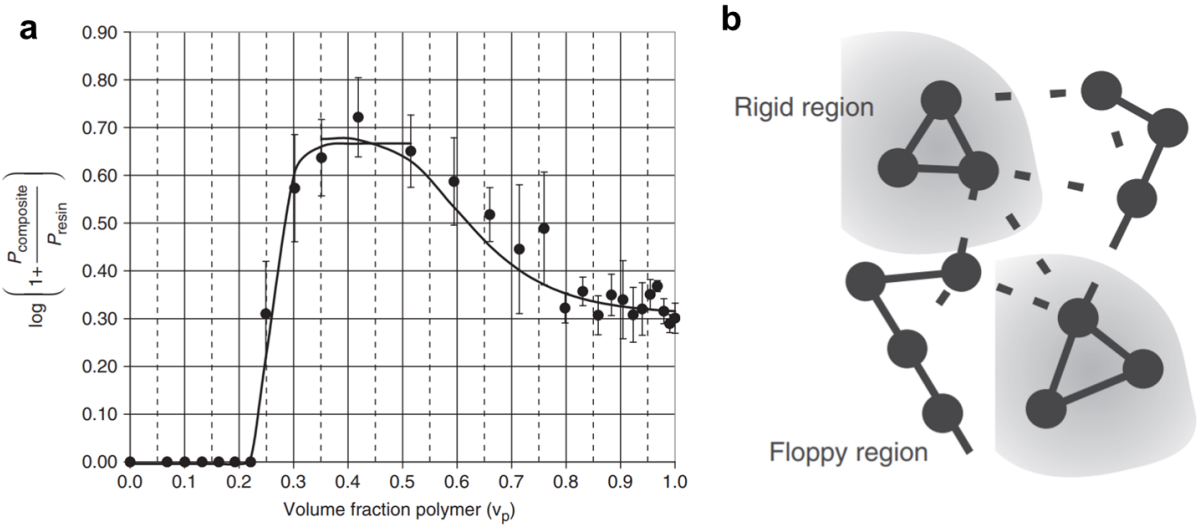

Figure 2.16: (a.) Modulus relative to pure resin properties as a function of volume fraction polymer and (b.) schematic diagram of floppy and rigid zones from Verbeek et al. [28].

polymer present to transform the network of particles into a rigid structure. As the ratio of rigid and floppy structures varies, as shown in Figure 2.16b the properties of the system will also vary. In addition, the significantly reduced chitosan content at 80% vol loading can greatly diminish the formation of the chitosan interphase needed for strong phase co-

continuity and measurable improvements to the mechanical properties. At 30 and 50% vol. SiC loading, stress transfer is improved due to the presence of more rigid regions connected by the surrounding chitosan matrix.

The crosslinking density of the co-continuous chitosan phase also has a role in the mechanical properties of the coatings. Although no crosslinker was added and the crosslink density was not measured for these samples, work by Zhenhua et al. on styrene-butadiene rubber (SBR) and carbon black nanocomposites demonstrated there exists an optimal crosslink density for a specific strengthening system[29]. At a constant (30%) carbon black nanofiller loading, the tensile strength vs. crosslinking density plot in Figure 2.17 shows that the tensile strength increases rapidly with increasing crosslinking density but falls off at a critical point. This decline is attributed to the gradually increasing intermolecular chemical bonding, which hinders the orientation and alignment of polymer chains among the particles when subject to external force[29]. To optimize the mechanical properties, a fine balance between crosslink density and particle-polymer chain interaction is required.

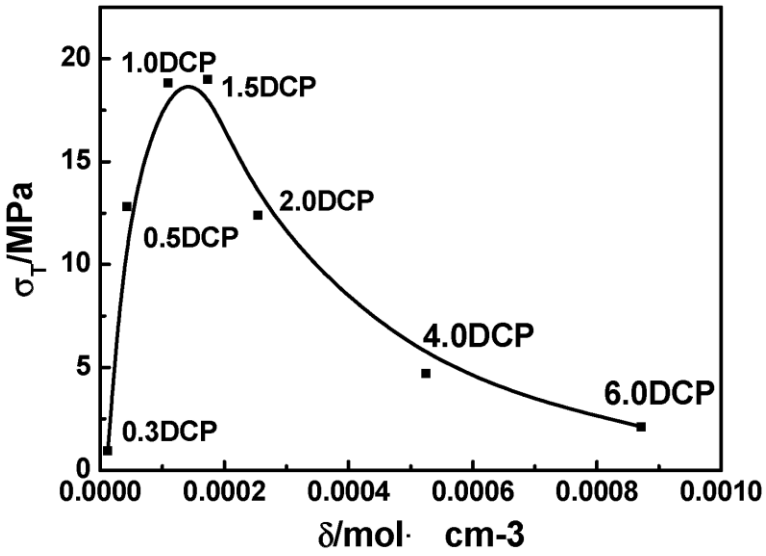

Figure 2.17: Effect of crosslinking density (δ) on the tensile strength (σ_T) of styrene-butadiene rubber (SBR) filled with 30% carbon black adapted from Zhenhua et al.[29].

2.4.3 Single Impact

As mentioned in the experimental procedure, the dynamic hardness module of the instrument provides the added benefit of measuring the depth of the indenter dynamically thanks to the high data acquisition rate (1-5MHz) of the instrument. Since the depth of the indenter is measured throughout the impact process, the instantaneous velocity of the indenter tip can also be extrapolated. From this data, the strain rate and the dynamic hardness of the samples can be calculated. Although the strain rate varies during the impact process, an average strain rate ($\boldsymbol{\varepsilon}$) can be approximated using the following equation

$$\varepsilon \approx \frac{V_{in}}{h_{max}} \tag{5}$$

where $\boldsymbol{V_{in}}$ is the initial contact velocity of the indenter measured at where the indentation depth crosses the zero point and $\boldsymbol{h_{max}}$ is the maximum depth of the indenter[30]. The position of values on a typical depth vs. time curve is shown in Figure 2.18. The average strain rate of these impacts is approximately 40 s^{-1}.

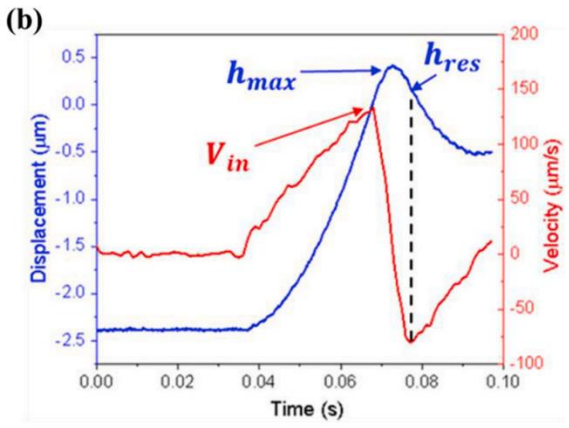

Figure 2.18: Representative indenter displacement (blue curve) and velocity (red curve) history from an impact test from Wang et al. [30].

The depth of the indenter at the initial contact point, depth of the indenter at the resting point, and amplitude of the indenter rebound off the sample surface can be used to determine the dominant mode of deformation. When comparing the typical depth vs time plot in Figure 2.9c against the depth vs time plot from the tested samples, in Figure 2.19, the lack of negative depth after initial contact and the increase of depth after the first

impact are key points to note. Under most conditions, it is generally assumed that the plastic deformation of the material is completed by the first contact cycle as the initial contact depth and the final depth are about the same [18], [30]. However, for the samples tested, there is a continued increase in the contact depth with each rebound of the indenter and no rebound away from the sample surface is measured. In comparison to the glass control sample plotted in yellow, we can see that the impact behavior between the two is drastically different.

The lack of rebound from the coated samples sufficient to overcome the constant 5mN accelerating load suggests that the coatings may also provide some damping capabilities in addition to impact resistance. This is further reinforced by the velocity vs time plots (Figure 2.19) which show that as SiC loading is increased, the coating's ability to

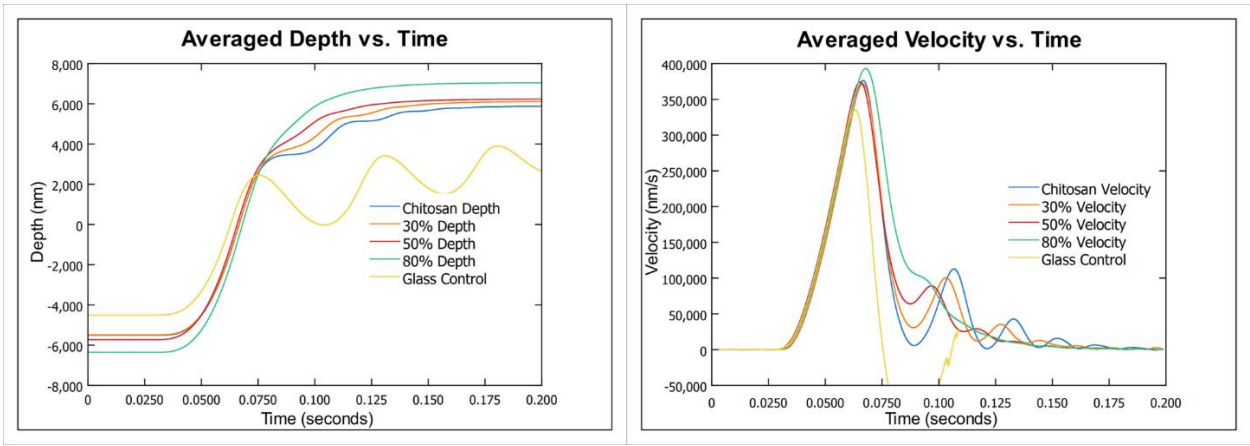

Figure 2.19: Averaged (10 samples) depth vs. time and velocity vs. time from the dynamic hardness module of the nano impact.

dampen the rebound oscillations of the indenter tip is also improved. In addition, the time in which the indenter comes to rest occurs sooner with higher particle loading. A similar study by Velmurugan et al. reports a similar trend when subjecting montmorillonite-polymer nanocomposites to low velocity impacts[31]. When it comes to resisting penetration from impacts, the impact depth is most greatly minimized with the pure

chitosan sample. The evolution of the impact depth after successive impacts will be investigated using the multiple impulse module of the instrument.

2.4.4 Multiple Impact

The operating principle for the multiple impulse module is similar to that of the dynamic hardness module, except each selected region is subjected to 100 successive impacts. This is done to observe the damage evolution of the sample. A typical depth vs time plot is shown in Figure 2.9b and the collected data from the prepared samples is plotted in Figure 2.20. 30% SiC particle loading is best at resisting penetration followed by

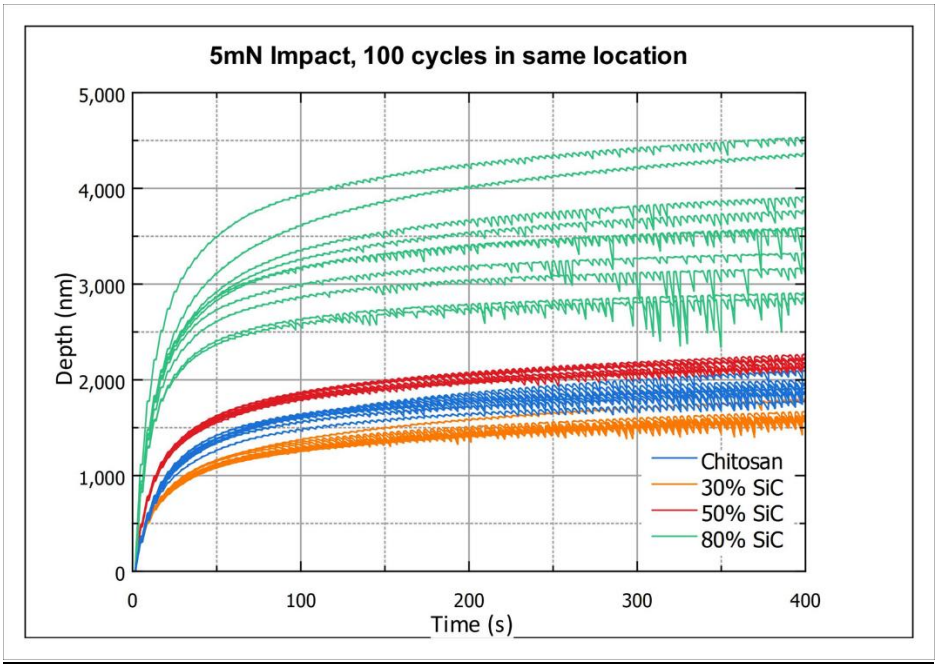

Figure 2.20: Depth vs. time plots from the multiple impulse module. Samples were subject to 100 5mN impacts over a duration of 400 seconds.

pure chitosan, 50% SiC, and then 80% SiC. This is most likely attributed to the higher chitosan phase content, which can better form the co-continuous phase needed to form a continuous network among the SiC nanofiller. The drastically wider variation in the final depth for 80% SiC samples is attributed to the much higher surface roughness and discontinuity of the chitosan matrix. Some regions may also contain localized regions with

more chitosan phase present than others, which puts them further above the rigidity percolation point and is better able to resist deformation.

2.4.5 SEM micrographs of the impact area

The deformation and damage to the film after 5mN single impacts are in Figure 2.21 and the deformation and damage to the film after 100 successive 5mN impacts are in Figure 2.22. From these micrographs and the evolution of the indenter depth, we can get a rough idea of the deformation-damage evolution. Upon initial contact, all the films undergo plastic deformation with visible nucleation of small stress cracks in the pure chitosan (Figure 2.21-2.22 a and c respectively) and 50% volume SiC sample. Coating and particle pileup surrounding the indenter tip is also observed. With additional impact cycles, the overall plastic deformation per impact is gradually suppressed as indicated by the reduction in additional impact depth per cycle in Figure 2.20, which furthers the growth of sub surface cracks. After 100 impacts, these subsurface cracks have coalesced, leading to film fracture. The increase in particle pileup surrounding the impact crater further validates the hypothesis that upon impact, the particles rotate and translate to dissipate the impact energy. The reduced impact depth observed for 30% volume SiC, in Figure 2.20 can be explained by better resistance to crack growth and coalescence, and eventual coating fracture. The triagonal shape of the impact crater (Figure 2.22a) for pure chitosan is due to early crack coalescence, followed by film fracture and the significant pileup surrounding the indenter tip after successive impacts. Unfortunately, due to sample delamination (Figure 2.21d inset), when exposed to the high vacuum of the SEM, the tested area of 80% volume SiC samples could not be imaged. The disjointed connectivity of chitosan here allows the shrinkage from sample drying under vacuum to easily tear the sample.

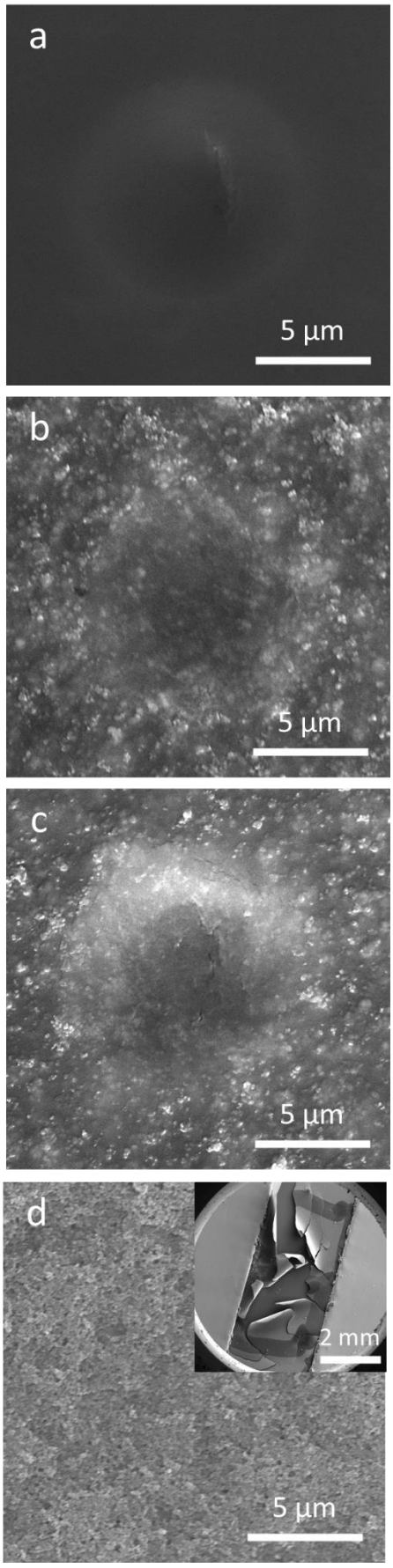

Figure 2.21: SEM micrographs of single 5mN impacts for (a.) pure chitosan, (b.) 30% volume SiC, (c.) 50% volume SiC, (d. inset) delamination of the 80% volume sample preventing imaging of the impact zone and (d.) surface of 80% volume SiC showing significantly diminished chitosan phase.

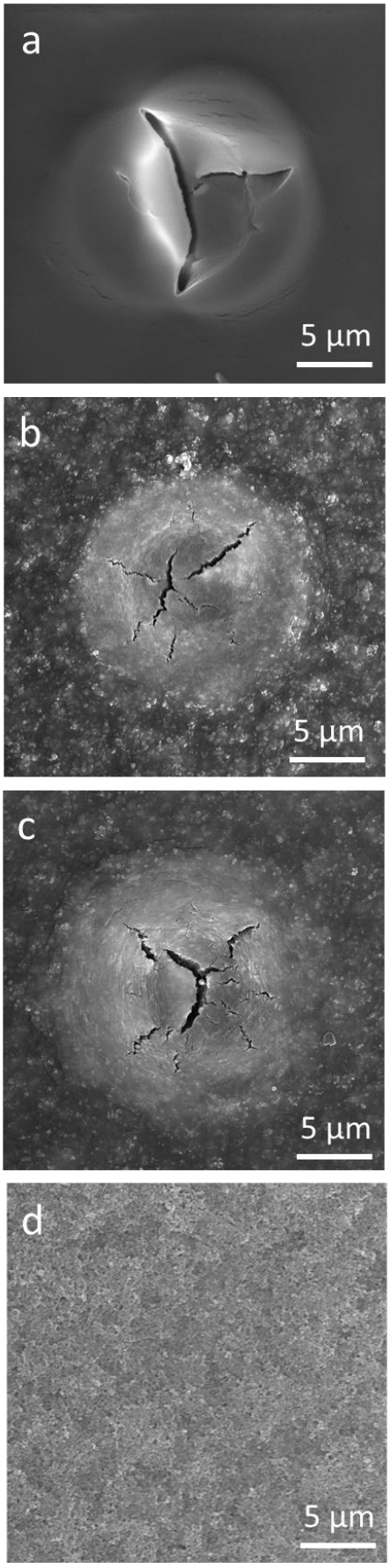

Figure 2.22: SEM micrographs of 100 5mN impacts for (a.) pure chitosan, (b.) 30% volume SiC, (c.) 50% volume SiC, and (d.) surface of 80% volume SiC without impact due to sample delamination.

Chapter 3: Drop cast coatings on quartz substrates subject to high loads

3.1 Objective

Nanomechanical testing at low peak loads was used to characterize both the quasi-static and dynamic properties of the nanocomposite protective film as a function of particle loading. It has helped us understand the mechanics of film during deformation at different strain rates without causing significant damage to the substrate itself. Because impact protective coatings are often sacrificial and can be reapplied, the capability of the coating to reduce damage on the substrate surface must also be investigated.

To accomplish this, multiple impulse nano impact testing was conducted with accelerating loads 20 fold higher (100mN) than the previous 5mN used in dynamic hardness mode. This was to ensure sufficient transmission of the applied impact energy and induce brittle fracture in the quartz substrate for the new set of SiC/Chitosan coatings. In addition to observing the impact damage to the coating, damage to the substrate will also be quantified after removal of the coating.

3.2 Experimental Procedure

3.2.1 Chitosan solution and SiC suspension preparation

1 % w/v chitosan solution was prepared by dissolving 0.1g of low molecular weight chitosan powder (50-190kDa Sigma 448869-50G) into 10mL of 1% v/v acetic acid solution overnight with stirring until the solution is homogeneous. The final pH is ~4.00.

1% w/v SiC suspension was prepared by adding 0.1 g of ~60nm spherical SiC particles into 10 mL of deionized water. 100 µL of HCI was then added to help prevent agglomeration of the SiC particles. To disperse the particles, the suspension was agitated via shaking and stirring within the vial and bath sonication using a Branson CPX2800 for

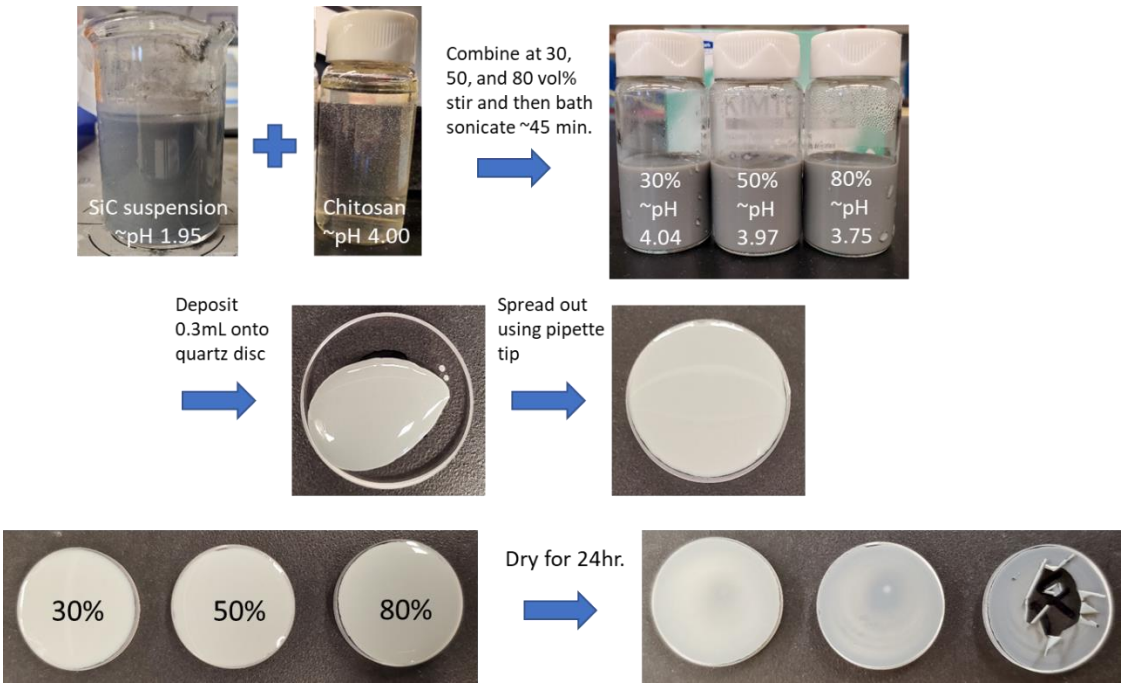

Figure 3.23: Diagram showing the coating deposition process onto quartz substrates. Peeling of the coating and non-homogeneity of the coating as observed in the bottom right represent some issues with the drop cast process.

45 minutes. Both the preparation of the chitosan solution and SiC suspension were performed under the fume hood due to the corrosive nature of the acetic acid and hydrochloric acid, and the inhalation risk of the SiC nanoparticles. The final pH of the SiC suspension is ~1.95.

To prepare the different volume percent of SiC loading (30, 50, and 80 vol. %), varying ratios of the chitosan solution and SiC suspension were combined and then tip sonicated for 2 min with physical agitation to endure homogeneous mixing.

3.2.2 Quartz disc preparation and coating deposition

Highly polished fused quartz discs (25.4mm diameter x 1.6mm thick) from Ted Pella (1600 1-1) were used as the substrate. Before deposition, the quartz discs were first cleaned with acetone and dried using a Kimwipe. Further cleaning to remove acetone residue was done using ethanol and then air dried. Before deposition, the sample was tip

sonicated to redisperse the SiC particles within the suspension. Then, 0.3mL of the prepared coating was then deposited using a micropipette. The decrease in deposited solution is to account for the smaller surface area of the quartz substrates to control the overall coating thickness. Due to the surface tension of the droplet as shown in Figure 3.23 the coating was then spread – with the micropipette tip - to cover the entire surface and left to dry overnight.

3.3 Characterization

3.3.1 Nano Impact

To better characterize the protective capability of the SiC/Chitosan thin film, 100 high strain rate impacts (~30 s^{-1}) with a 100mN accelerating load and 10000nm accelerating distance was used to test the reprepared coatings on quartz substrates. Three regions spaced 150 micrometers apart were done to account for variation in the coatings and prevent the overlap of adjacent strain fields from previous impacts.

3.4 Results and Discussion

3.4.1 Potential causes for coating delamination

To investigate the morphology of the coatings and their homogeneity, the coatings were imaged using SEM. As shown in Figure 3.24c, the thickness of the coatings was found to be ~5-10μm. This is close to the thickness of the previous film, which suggests that thickness can be controlled as a function of deposition. A cross sectional view of the film and a surface view of the film shows that the distribution of SiC particles within the chitosan matrix is homogeneous and did not experience settling during the drying process at the microscopic scale. As expected, less of the chitosan network was observed in coatings with higher (50% and 80% vol. SiC) SiC content in Figure 3.24e and 3.24f respectively.

However, at a macroscopic scale, the formation of "coffee rings" can be observed in the finished product shown in Figures 3.23 and 3.24b. We believe that a major factor contributing to "coffee ring" formation is the long drying times, which allow capillary flow within the deposited droplet to carry the SiC particles towards the outer edge[32]. Deegan et al. reported that liquid evaporating at the pinned solid-liquid contact line is replenished by liquid from the interior, drawing microspheres towards the edge[32]. The SiC+Chitosan coatings do not form a well-defined "coffee ring" perimeter due to the gradually reduced mobility of SiC nanoparticles as the solvent evaporates during the drying process. As the solvent evaporates, the viscosity of the chitosan increases as the water content decreases and forms a thin film. To ensure that the entire substrate is evenly protected, it is necessary to develop methods to improve coating homogeneity.

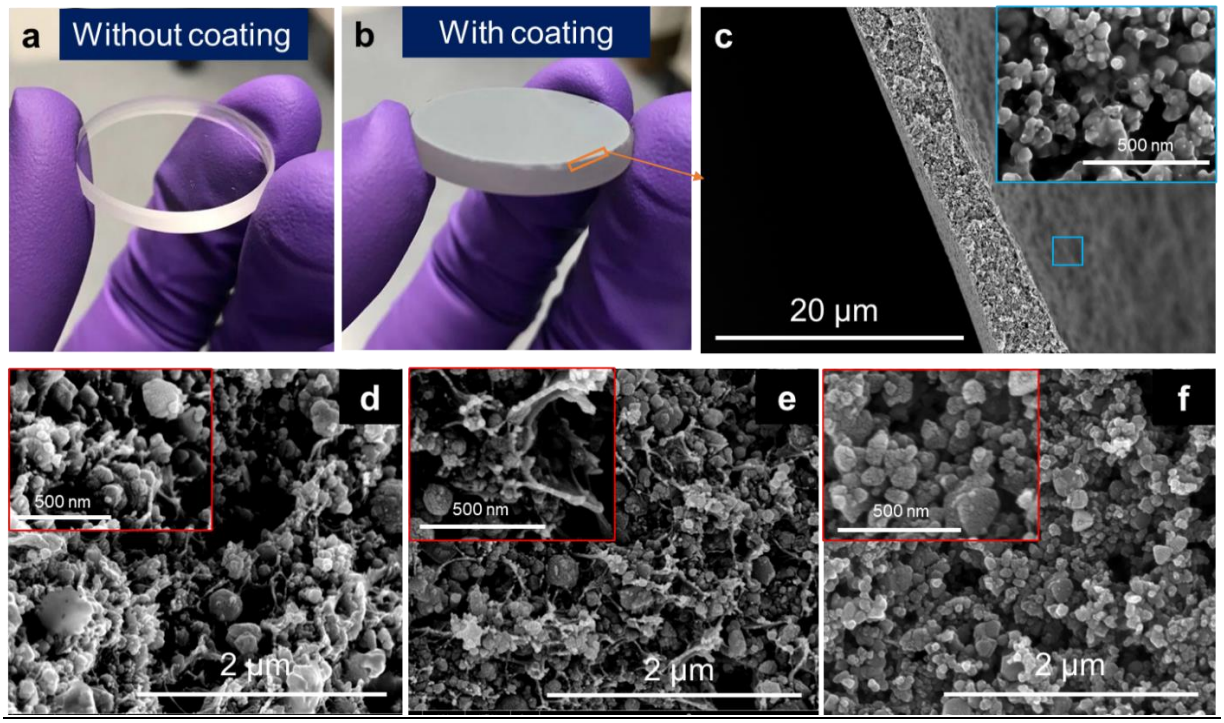

Figure 3.24: Quartz discs a with and b without SiC/Chitosan nanocomposite coating. Under SEM, the cross section (c.) of the coating was observed to determine the thickness and homogeneity. The surface morphology of (d.) 30%, (e.) 50%, and (f.) 80% vol. loading was also observed.

After coating application and drying, “mud crack” formation and curling of the coating away from the quartz substrate would sometimes occur in coatings with higher SiC content (Figure 2.21d inset and 3.23). Bi-axial tensile stresses are generated as the shrinkage of the coating becomes constrained by the rigid substrate. When the tensile stress within the film exceeds the material dependent critical stress, cracking occurs[33]. Curling of the coating away from the substrate serves as a secondary mechanism to reduce the energy within the film by generating new surfaces between the film and the substrate[34]. At higher SiC concentrations, there is insufficient chitosan presence to form dense polymer networks. Furthermore, SiC nanoparticles could potentially limit the interactions between neighboring chitosan monomers, resulting in a weaker polymer network. As seen in Figures 2.21, 2.22, and 3.24, coatings containing 80% vol. SiC more closely resemble that of individual particles than particles immersed within a matrix. Modification of the binder, chitosan, or solvent amount can help control the formation of such defects. Previous studies in adding nano-scale functional fillers to polymers have reported that the interphase has a significant contribution to the improved modulus due to their relatively high volume percentage of the total composite[24], [35].

3.4.2 Multiple Impulse Nano-Impact

Observation of the damage occurring at the coating surface can help us understand the energy dissipation mechanisms. In Figure 3.25 SEM micrographs of the impact area on prepared samples show the differing energy dissipation mechanisms and damage area radius (R_d) after testing. In the sample without any coating, brittle fracture and large cracks were observed. In samples with SiC/Chitosan coatings, SiC nanoparticle pile up and microcracks are the main energy dissipation mechanisms. This is in line with what is

observed in the impact region of the dactyl club. Although the penetration depth in all the samples is similar, the radius of the damaged area is significantly reduced in samples with 50 vol% SiC/Chitosan coatings. Microcrack propagation is most pronounced on the 80% volume sample due to the lack of a percolated polymer network. Here, many voids are present in between the SiC particles, which leads to poor stress transfer and lack of cohesion. Reduction in mechanical properties well before the ~88% vol loading of bi-continuous hydroxyapatite nanoparticles found in the dactyl club of the mantis shrimp, strongly suggests that the bi-continuity of the particles have a significant role in improving the connectivity of the polymer network and strength of the interphase. Furthermore, due to their bi-continuous nature, the particles may occupy 88% volume, but may be only comprised of a significantly reduced ceramic phase due to interpenetrating protein and chitin matrix.

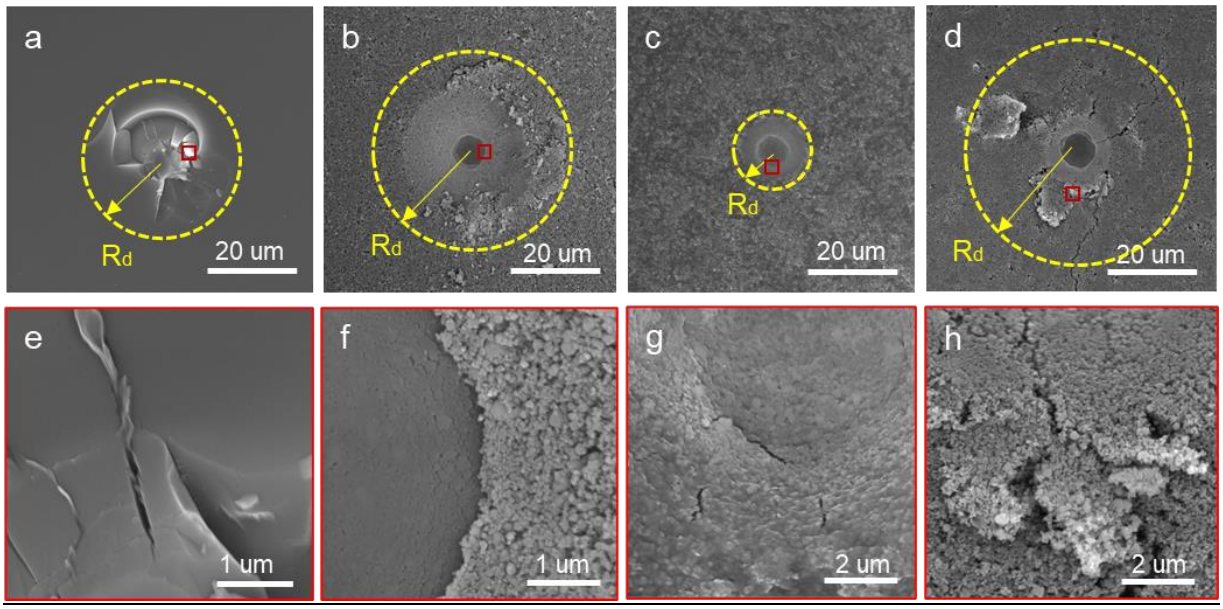

Figure 3.25: Nanoimpact tests on quartz samples with and without SiC/chitosan coatings. (a.-d.) SEM images of indents in different samples. (a.) No coating; (b.) 30 vol%; (c.) 50 vol%; and (d.) 80 vol%. (e.-h.) high magnification SEM images of indent damages.

From the previous nanoindentation data and measurement of the impact area at the surface of the coating, coatings with 50% volume SiC possess both the highest reduced modulus and hardness in addition to the smallest damage area on the surface. Subsequent removal of the coating from the quartz shows that the damaged area (Figure 3.26), is reduced by ~49.1% with just the pure chitosan coating and by ~72.2% with 50% vol. SiC

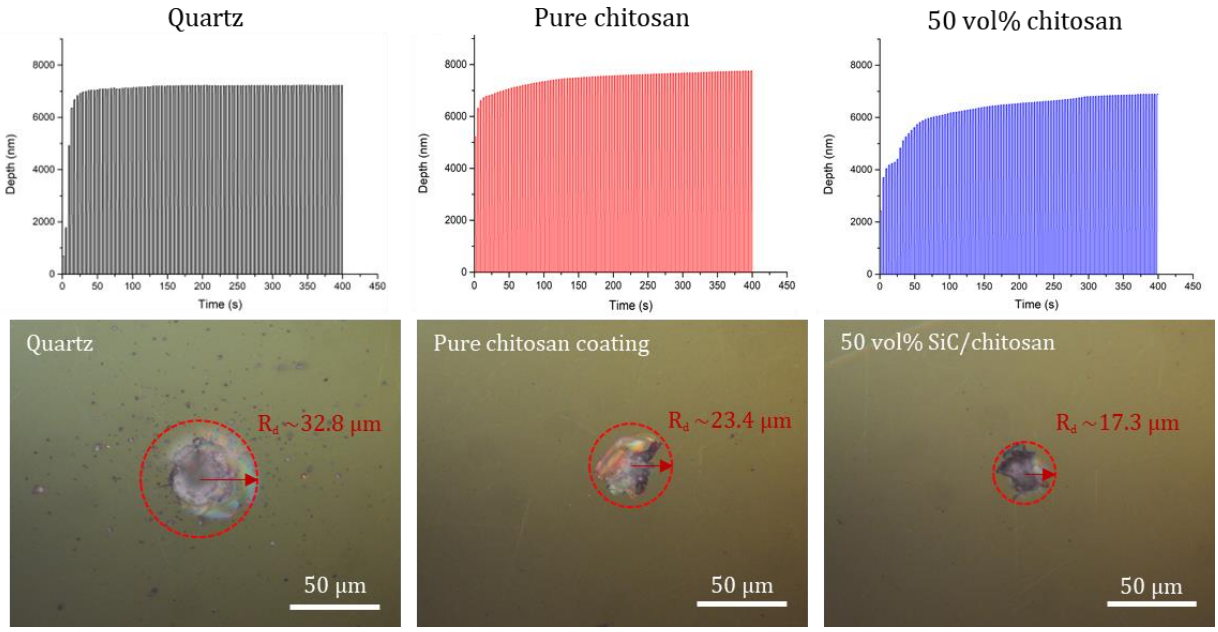

Figure 3.26: First row, depth vs. time data obtained after 100 100mN impacts in the same area for quartz, pure chitosan, and 50% vol. SiC particles. Second row, OM micrographs of the impact region with the measured impact radius (R_d).

loading when compared to uncoated quartz. Depth vs time plots (Figure 3.26) show that the addition of hard SiC nanoparticles can also improve the impact resistance of protective coatings as it took more impacts before the penetration depth into the sample began to plateau. In conclusion, these nano impact results demonstrated that thin SiC/chitosan nanocomposite coatings can provide adequate protection for brittle ceramic substrates against high strain-rate impacts.

Chapter 4: Preliminary results on improving coating uniformity and homogeneity via spray casting

4.1 Objective

High load nano impact testing on coatings demonstrates that the coatings have good protective ability against high strain rate impacts. However, shortcomings such as low homogeneity, poor particle dispersion, non-uniform thickness, and delamination of the coating hinder the coating's ability to uniformly protect the substrate. This not only impedes the core functionality of the coating but also presents a challenge toward scalability. The long evaporation times and water like viscosity prevent application on objects with complex geometries or objects with vertical or overhanging geometries while also promoting the formation of coffee rings. To overcome these shortcomings, the application of the coating via pneumatic spraying was evaluated. Application using this method, combined with heating of the substrate, allows successive thin layers to be deposited. This process reduces the evaporation time from hours to seconds, which improves uniformity by impeding coffee ring formation. Further improvements to reducing manufacturing process variability are also being addressed via the creation of the computer controlled pneumatic spraying system.

4.2 Experimental Procedure

4.2.1 Solution preparation

To prepare a large quantity of 2% w/v chitosan, 1.6g of low molecular weight chitosan powder (50-190kDa Sigma 448869-50G) into 80mL of a 2% v/v acetic acid solution. Under vigorous stirring (1250RPM), the solution was heated to 50°C for 1 hour to accelerate the process. The final solution may also require degassing under vacuum to improve the clarity. After the solution has cooled, 3% w/w equal to chitosan weight, or 0.048g, of citric acid (Sigma 251275-100G) was added to act as a crosslinker.

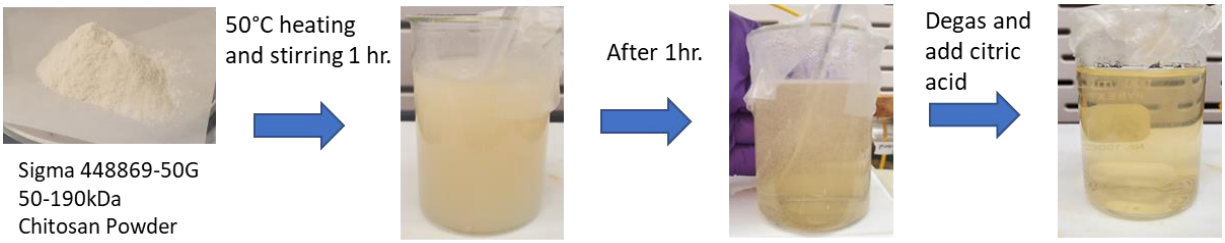

Figure 4.27: 2% w/v Chitosan solution preparation process.

To match the increase in chitosan % w/v, a 2 % w/v SiC suspension was made by mixing 1.6g of 60nm SiC nanoparticles into 80 mL of DI water. Then, 0.024mL of 35% HCL was added to prevent the aggregation of the SiC particles. To disperse the SiC particles, the solution was tip sonicated for 5 minutes with a plunging action to push all the particles on the surface into the suspension. After tip sonication, the suspension was placed on a stir plate to prevent settling.

Figure 4.28: 2% w/v SiC suspension preparation process.

Similar to before, varying ratios (30, 50, and 80 vol. % SiC) of the chitosan solution to SiC suspension were combined and then tip sonicated for 2 min with physical agitation to endure homogeneous mixing.

4.2.2 Quartz disc preparation

Highly polished fused quartz discs (25.4mm diameter x 1.6mm thick) from Ted Pella (16001-1) were used as the substrate. Before deposition, the quartz discs were first

cleaned with acetone and dried using a Kimwipe. Further cleaning to remove acetone residue was done using ethanol and then air dried.

4.2.3 Spray cast deposition

Cleaned quartz substrates were placed onto a hotplate heated to 120°C and secured using paper tape to prevent substrate movement from the air pressure of the spray gun.

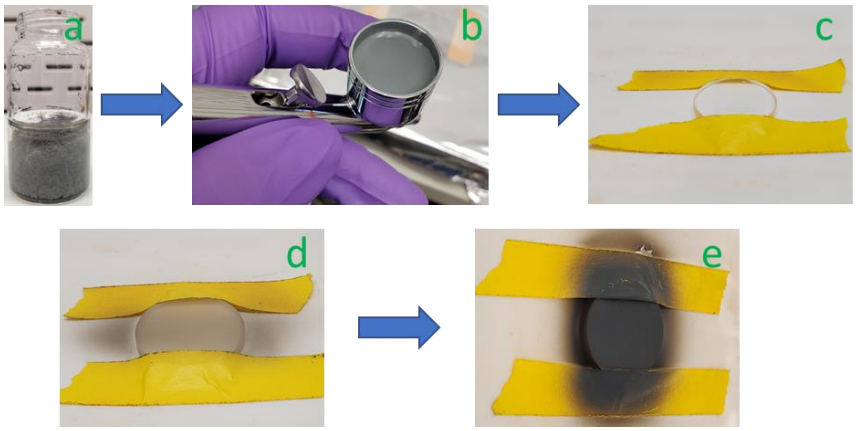

Figure 4.29: (a.) Prepared coating solution before tip sonication, (b.) sonicated solution placed into air brush hopper, (c.) quartz disc on the hotplate before application secured by tape, (d.) coating appearance and uniformity before all layers are deposited, and (e.) the final product after coating deposition.

Prior to spraying, all prepared solutions were tip sonicated again to improve the homogeneity of the mixture. 1 mL of the prepared solution was pipetted into the hopper of the spray gun. More solution was applied during the spray coating process to account for loss caused by overspray. With the spray gun pressure set to 20 PSI, successive layers of the coating were applied until the hopper was emptied. The sample was then removed from the hot plate and set to cool to room temperature.

4.3 Results and Discussion

Based on preliminary testing from this modified application procedure and solution formula, this method can be used to apply SiC/Chitosan films at different volume fractions of SiC particle loading with high thickness uniformity and high dispersity. This increase in homogeneity also seems to reduce the tendency for the films to delaminate from the

substrate. Little to no delamination was observed after the coating drying or even weeks after deposition. A comparison between drop cast and spray cast coatings is depicted in Figure 4.30 in addition to spray cast coatings at 30%, 50%, and 70% volume fraction SiC nanoparticle loading. To further reduce process variability, the creation of a computer-controlled air brush for spraying coatings onto substrates for testing is also currently in progress (Figure 4.31). Due to the complex nature of spray deposition and high error in human application, computer-controlled deposition would allow us to further enhance coating thickness and dispersion, while also facilitating future systematic studies of changes to coating performance as a function of spray parameters (nozzle geometry, pressure, overlap, distance, and drying rate).

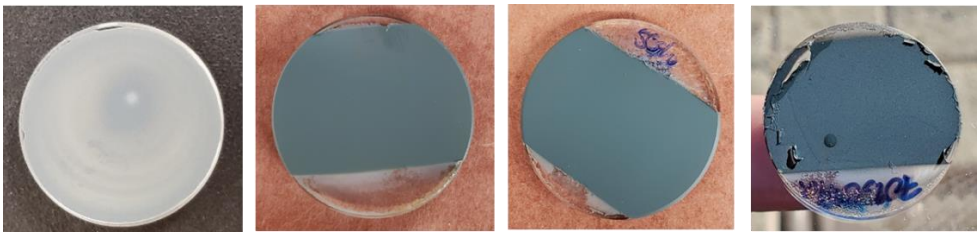

Figure 4.30: Comparison between 50% volume SiC drop cast coating (left) and sprayed samples with (left to right) 30%, 50%, and 70% volume SiC content.

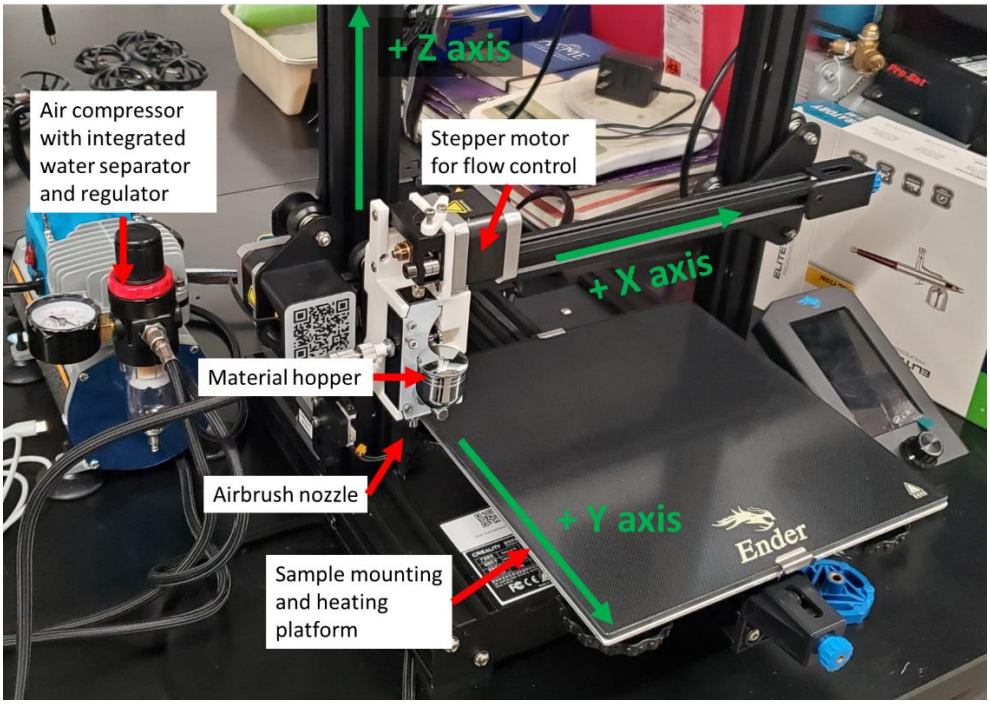

Figure 4.31: Schematic of computer controlled spraying machine adapted from a 3D printer.

Chapter 5: Future Outlook

Drawing inspiration from the mantis shrimp's nanocomposite impact resistant coating, we have successfully created our own synthetic analog comprised of solid ~60 nm SiC nanoparticles embedded within an organic chitosan matrix. From this, we were able to test our hypothesis and confirm that the impact resistance, hardness, and reduced modulus do increase as a function of increased particle loading, but only up to a certain extent. Characterization via quasi-static indentation and high strain rate nano impact testing also allowed us to confirm our hypothesized energy dissipation mechanisms and observe the damage evolution after repeated impacts. Although the preliminary data presented is very exciting, more work must be done to more closely emulate the mesocrystalline and bi-continuous nature of the HAP nanoparticles found on the dactyl club.

Incorporation of mesocrystalline materials into the nanocomposite may provide a pathway to control the energy dissipation capability of the coating by altering the fracture toughness of the nanoparticles used. The coatings could be tailored such that additional energy dissipation, via particle fracture, only occurs after the desired amount of impact energy has struck the substrate. This could provide additional protection without significantly increasing the thickness or weight of the coating. The 88% volume occupied by the bi-continuous hydroxyapatite nanoparticles is only partially comprised of solid hydroxyapatite phase, with the rest being occupied by an interpenetrating network of chitin and protein matrix. Incorporation of bi-continuous particles, perhaps by studying the mineralization process in the mantis shrimp to guide particle growth synthesis, would allow for potentially higher particle loading due to higher matrix continuity and interfaces between the nanoparticles and matrix. This could potentially allow for > 50% volume

particle loading without surpassing the rigidity percolation point where no observable mechanical benefit can be observed. In addition to changing the morphology of the constituent materials, changing the materials used in the nanocomposite could also yield additional benefits in the form of multifunctionality.

We used SiC nanoparticles and chitosan for our nanocomposite coatings. However, transitioning to coatings comprised of other nanoparticles and matrices, such as those that are resistant to high temperatures, thermally insulative, have piezoelectric properties, or are optically transparent, could further extend the operating range of the coatings, allowing them to be applied to extreme environments or even have sensing capabilities that can detect where damage has occurred on the substrate, or be applied to lenses for protection. The use of matrices with different viscoelastic or non-Newtonian behavior could extend the range of impact energies the coating can protect against by stiffening or softening depending on the strain rate.

Before the SiC/Chitosan coatings can see widespread use, much more work also needs to be done to validate the protective capabilities of the coating when exposed to real world environments and degradation from age. The coating's abrasion/wear resistance, adhesive strength, susceptibility to moisture or other solvents, and effect of processing parameters have yet to be tested and characterized. Strong performance in these tests helps ensure the long life and consistent protective capability of the coating. In the near future, I hope to test these parameters using the scratch and wear testing capabilities of nanoindentation in addition to creating custom tools and processes to manufacture these coatings. I have already begun my first steps in improving by creating a computer-

controlled coating application platform by modifying a 3D printer. With it, I hope it will improve the consistency, efficiency, and scale, in which I can test the effect of thickness, spray parameters, drying rate, and different coating materials. I hope to continue this in Dr. David Kisailus' lab under the Materials and Manufacturing Technology department.

REFERENCES

[1] N. P. Padture, M. Gell, and E. H. Jordan, "Thermal Barrier Coatings for Gas-Turbine Engine Applications," vol. 296, no. April, pp. 280–285, 2002.

[2] A. Popoola, O. Olorunniwo, and O. Ige, "Corrosion Resistance Through the Application of Anti- Corrosion Coatings," *Dev. Corros. Prot.*, 2014, doi: 10.5772/57420.

[3] K. Pugh, G. Rasool, and M. M. Stack, "Raindrop Erosion of Composite Materials: Some Views on the Effect of Bending Stress on Erosion Mechanisms," *J. Bio- Tribo-Corros.*, vol. 5, no. 2, p. 45, Jun. 2019, doi: 10.1007/s40735-019-0234-8.

[4] "3M wind blade protection coating W4600," p. 2.

[5] L. Li and C. Ortiz, "Pervasive nanoscale deformation twinning as a catalyst for efficient energy dissipation in a bioceramic armour," *Nat. Mater.*, vol. 13, no. 5, pp. 501–507, May 2014, doi: 10.1038/nmat3920.

[6] W. Huang *et al.*, "A natural impact-resistant bicontinuous composite nanoparticle coating," *Nat. Mater.*, vol. 19, no. 11, pp. 1236–1243, Nov. 2020, doi: 10.1038/s41563-020-0768-7.

[7] S. N. Patek and R. L. Caldwell, "Extreme impact and cavitation forces of a biological hammer: strike forces of the peacock mantis shrimp *Odontodactylus scyllarus*," *J. Exp. Biol.*, vol. 208, no. 19, pp. 3655–3664, Oct. 2005, doi: 10.1242/jeb.01831.

[8] N. A. Yaraghi, N. Guarín-Zapata, L. K. Grunenfelder, E. Hintsala, S. Bhowmick, and ..., "A sinusoidally architected helicoidal biocomposite," *Adv. Mater.*, vol. 28, no. 32, pp. 6835–6844, 2016.

[9] A. Muxika, A. Etxabide, J. Uranga, P. Guerrero, and K. de la Caba, "Chitosan as a bioactive polymer: Processing, properties and applications," *Int. J. Biol. Macromol.*, vol. 105, pp. 1358–1368, 2017, doi: 10.1016/j.ijbiomac.2017.07.087.

[10] S. Y. Park, K. S. Marsh, and J. W. Rhim, "Characteristics of different molecular weight chitosan films affected by the type of organic solvents," *J. Food Sci.*, vol. 67, no. 1, pp. 194–197, 2002, doi: 10.1111/j.1365-2621.2002.tb11382.x.

[11] J. L. Shamshina, T. Oldham (Konak), and R. D. Rogers, *Applications of Chitin in Agriculture*. 2019. doi: 10.1007/978-3-030-16581-9_4.

[12] P. Guerrero, A. Muxika, I. Zarandona, and K. de la Caba, "Crosslinking of chitosan films processed by compression molding," *Carbohydr. Polym.*, vol. 206, no. November 2018, pp. 820–826, 2019, doi: 10.1016/j.carbpol.2018.11.064.

[13] O. J. Pemble, M. Bardosova, I. M. Povey, and M. E. Pemble, "A slot-die technique for the preparation of continuous, high-area, chitosan-based thin films," *Polymers*, vol. 13, no. 10, pp. 1–13, 2021, doi: 10.3390/polym13101566.

[14] H. Abderrazak and E. S. B. Hadj Hmi, "Silicon Carbide: Synthesis and Properties," in *Properties and Applications of Silicon Carbide*, R. Gerhardt, Ed. InTech, 2011. doi: 10.5772/15736.

[15] I. Younes and M. Rinaudo, "Chitin and chitosan preparation from marine sources. Structure, properties and applications," *Mar. Drugs*, vol. 13, no. 3, pp. 1133–1174, 2015, doi: 10.3390/md13031133.

[16] J. G. Fernandez and D. E. Ingber, "Manufacturing of large-scale functional objects using biodegradable chitosan bioplastic," *Macromol. Mater. Eng.*, vol. 299, no. 8, pp. 932–938, 2014, doi: 10.1002/mame.201300426.

[17] W. C. Oliver and G. M. Pharr, “An improved technique for determining hardness and elastic modulus using load and displacement sensing indentation experiments,” no. 1, 1992.
[18] X. Shi, J. Chen, B. D. Beake, T. W. Liskiewicz, and Z. Wang, “Dynamic contact behavior of graphite-like carbon films on ductile substrate under nano/micro-scale impact,” *Surf. Coat. Technol.*, vol. 422, p. 127515, Sep. 2021, doi: 10.1016/j.surfcoat.2021.127515.
[19] S. Watcharotone *et al.*, “Interfacial and Substrate Effects on Local Elastic Properties of Polymers Using Coupled Experiments and Modeling of Nanoindentation,” *Adv. Eng. Mater.*, vol. 13, no. 5, pp. 400–404, May 2011, doi: 10.1002/adem.201000277.
[20] T. Y. Tsui and G. M. Pharr, “Substrate effects on nanoindentation mechanical property measurement of soft films on hard substrates,” *J. Mater. Res.*, vol. 14, no. 1, pp. 292–301, Jan. 1999, doi: 10.1557/JMR.1999.0042.
[21] G. M. Pharr and W. C. Oliver, “Measurement of Thin Film Mechanical Properties Using Nanoindentation,” *MRS Bull.*, vol. 17, no. 7, pp. 28–33, Jul. 1992, doi: 10.1557/S0883769400041634.
[22] P. Rittigstein, R. D. Priestley, L. J. Broadbelt, and J. M. Torkelson, “Model polymer nanocomposites provide an understanding of confinement effects in real nanocomposites,” *Nat. Mater.*, vol. 6, no. 4, pp. 278–282, Apr. 2007, doi: 10.1038/nmat1870.
[23] “All About Soda Lime Glass - Composition and Properties.” https://www.thomasnet.com/articles/plant-facility-equipment/soda-lime-glass/ (accessed Nov. 20, 2022).
[24] A. K. Naskar, J. K. Keum, and R. G. Boeman, “Polymer matrix nanocomposites for automotive structural components,” *Nat. Nanotechnol.*, vol. 11, no. 12, pp. 1026–1030, Dec. 2016, doi: 10.1038/nnano.2016.262.
[25] E. Senses and P. Akcora, “An Interface-Driven Stiffening Mechanism in Polymer Nanocomposites,” *Macromolecules*, vol. 46, no. 5, pp. 1868–1874, Mar. 2013, doi: 10.1021/ma302275f.
[26] C. J. R. Verbeek, “Effect of Percolation on the Mechanical Properties of Sand-filled Polyethylene Composites,” *J. Thermoplast. Compos. Mater.*, vol. 20, no. 2, pp. 137–149, Mar. 2007, doi: 10.1177/0892705707073084.
[27] S. T. Knauert, J. F. Douglas, and F. W. Starr, “The effect of nanoparticle shape on polymer-nanocomposite rheology and tensile strength,” *J. Polym. Sci. Part B Polym. Phys.*, vol. 45, no. 14, pp. 1882–1897, Jul. 2007, doi: 10.1002/polb.21176.
[28] C. J. R. Verbeek, “Effect of percolation on the mechanical properties of sand-filled polyethylene composites,” *J. Thermoplast. Compos. Mater.*, vol. 20, no. 2, pp. 137–149, 2007, doi: 10.1177/0892705707073084.
[29] Z. Wang, J. Liu, S. Wu, W. Wang, and L. Zhang, “Novel percolation phenomena and mechanism of strengthening elastomers by nanofillers,” *Phys. Chem. Chem. Phys.*, vol. 12, no. 12, p. 3014, 2010, doi: 10.1039/b919789c.
[30] H. Wang, J. Thomas, M. A. Okuniewski, and V. Tomar, “Constitutive modeling of δ-phase zircaloy hydride based on strain rate dependent nanoindentation and nano-scale impact dataset,” *Int. J. Plast.*, vol. 133, p. 102787, Oct. 2020, doi: 10.1016/j.ijplas.2020.102787.
[31] R. Velmurugan, P. Jeyaprakash, and G. Balaganesan, “DAMPING STUDY OF HYBRID NANO COMPOSITES BY LOW VELOCITY IMPACT,” p. 4.

[32] R. D. Deegan, O. Bakajin, and T. F. Dupont, “Capillary flow as the cause of ring stains from dried liquid drops,” pp. 827–829, 1997.
[33] E. Santanach Carreras, F. Chabert, D. E. Dunstan, and G. V. Franks, “Avoiding ‘mud’ cracks during drying of thin films from aqueous colloidal suspensions,” *J. Colloid Interface Sci.*, vol. 313, no. 1, pp. 160–168, 2007, doi: 10.1016/j.jcis.2007.03.076.
[34] W. Meng, M. Liu, Y. Gan, L. Pauchard, and C. Q. Chen, “Cracking to curling transition in drying colloidal films,” *Eur. Phys. J. E*, vol. 43, no. 10, 2020, doi: 10.1140/epje/i2020-11985-4.
[35] A. Z. Zakaria and K. Shelesh-Nezhad, “The Effects of Interphase and Interface Characteristics on the Tensile Behaviour of POM/CaCO3 Nanocomposites,” *Nanomater. Nanotechnol.*, vol. 4, p. 17, Jan. 2014, doi: 10.5772/58696.